



OVERVIEW NO. 120

THE THERMOMECHANICAL INTEGRITY OF THIN FILMS AND MULTILAYERS

A. G. EVANS¹ and J. W. HUTCHINSON²¹Materials Department, College of Engineering, University of California, Santa Barbara, CA 93106-5050 and ²Division of Applied Sciences, Harvard University, Cambridge, MA 02138, U.S.A.

(Received 15 July 1994)

Abstract—Thin films and multilayers comprised of different classes of material are often used for various functional requirements. As these become relatively large in section and geometrically more complex, thermomechanical integrity is a major concern. It influences performance, yield and reliability. A methodology for thermomechanical design is needed that complements procedures used for circuit design. This article elaborates the principles of fail-safe thermomechanical design, based on the damage mechanisms known to occur in these systems. Among the important mechanisms are delamination and crazing of brittle layers, thermomechanical fatigue of metallic constituents and interface decohesion.

The damage mechanisms are generally activated by residual stress, both thermal and 'intrinsic'. The origins of these stresses are discussed, as well as stress redistribution effects that arise because of bending, discontinuities, etc. Emphasis is given to measurement methods which provide those data needed for implementation of the fail-safe design methodology.

1. INTRODUCTION

There are many technologies that use thin layers of dissimilar materials in order to achieve functional requirements. Some of the important areas include: electronic packaging [1] and ferroelectric actuators [2], as well as coatings used for either thermal protection [3] or for abrasion [4], oxidation and corrosion resistance. An example of a multilayer used for electronic packaging is shown in Fig. 1.1, to illustrate the variety of geometric arrangements that arise [1]. The dissimilar nature of the constituents presents challenges concerning the thermomechanical integrity and reliability [5], especially when at least one of the constituents is brittle: ceramic, semiconductor, glass, or certain polymers. Two dominant

factors causing reliability problems are the mismatch in thermal expansion coefficient between the materials, which causes residual stress, and the decohesion resistance of the interfaces. When one of the constituents is metallic, an additional factor is boundary layer shear that arises as a result of plasticity. Other significant phenomena include stress redistribution and thermomechanical fatigue. The intent of this article is to establish the principles governing the thermomechanical integrity of multilayers and to provide a methodology for designing fail-safe systems. It complements three other review articles: one on residual stress [6], a second on the mechanics of decohesion in multilayers [7] and a third on thin films [8].

Interfaces have a special significance in multilayer systems, because they are both numerous (Fig. 1.1) and susceptible to decohesion and sliding. A thermo-mechanical description of interfaces is provided, with an emphasis on decohesion and sliding characteristics. A particular challenge is the design and implementation of test procedures that measure interface properties. Few methods provide rigorous results which can also be readily implemented on actual multilayer configurations (Fig. 1.1). The methods which satisfy these requirements are emphasized and typical results discussed.

Residual stresses arise because of either thermal expansion differences between the constituents or defect annihilation subsequent to deposition [6, 8]. They are modified by various relaxation and

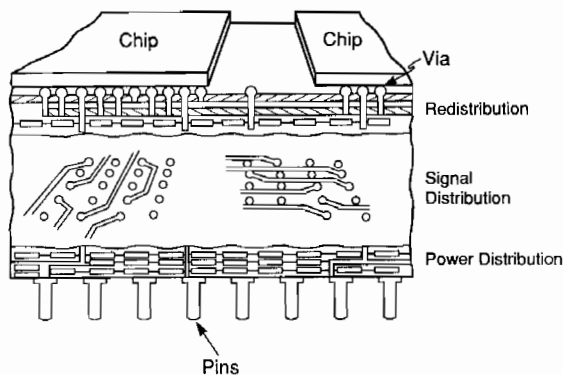


Fig. 1.1. A multilayer electronic package.

redistribution effects that occur as a result of creep and yielding, in addition to debonding and sliding at interfaces. There are also important effects on the stress of thermal cycling, especially when one constituent is metallic and when the temperature range is large enough to cause yielding. Redistribution phenomena are prevalent near edges and corners and in the presence of microcracks in the brittle layers. In consequence, the stresses cannot generally be predicted. Experimental procedures are needed to measure them. Moreover, the residual stresses are configuration dependent, because the plastic strains occur in response to the deviatoric stresses. There are particularly large differences between the stress magnitudes in planar layers compared with built-in cylindrical features, such as vias in electronic packages [9] (Fig. 1.1). Residual stress measurement techniques amenable to multilayers are described in this article.

The cracking and decohesion events expected in a multilayer system can be predicted, subject to knowledge about residual stresses, their redistribution, and the external loads, as well as the interface response. Many of these phenomena and the associated mechanics have been comprehensively addressed in a recent review [7]. In this article, an overview is given, including some additional phenomena. The primary importance of the mechanics is to define *fail-safe multilayer designs*. Such designs refer to multilayers that are incapable of thermostructural failure from the residual stresses existing in the system.

It is a common misconception that to ensure reliable performance, it is sufficient to have the brittle material be subject to in-plane compression. Such stresses indeed suppress cracking through the layer, *normal* to the interface, often referred to as crazing. But cracking may still occur *parallel* to the interface, resulting in delamination [7]. While both crazing and delamination can be suppressed by diminishing the residual stress, this is not always either possible or desirable, because the choice of materials and the processing are dictated by functionality considerations. Moreover, in principle, susceptibility to damage can also be diminished by reducing layer thicknesses [7]. But, this approach often introduces additional interfaces which frequently cause other problems, such as interface decohesion, dielectric breakdown, etc. [5]. In general, therefore, it is important to have a procedure for designing thermostructurally fail-safe multilayer systems, when there are functionality constraints on both the choice of materials and the layer thicknesses.

In many cases, the loading is cyclic and thermomechanical fatigue effects arise [10–13]. Among the important cyclic phenomena are shake-down and ratcheting, as well as the nucleation and growth of cracks near the interfaces. It is critically important to include these effects in the design methodology for multilayers.

2. RESIDUAL STRESS

2.1. Basic features

One source of residual stress is the thermal expansion mismatch between constituents. This mismatch leads to stresses when the temperature changes. There are other sources of residual stress when the layers are either vapor deposited or structurally modified at low homologous temperatures. These are often referred to as 'intrinsic' stresses. Such stresses develop as a consequence of diffusional effects in previously deposited sections of the film. They involve mechanisms which *eliminate defects* having an associated 'free volume' [6]. These defects include grain boundaries, vacancies, interstitials, voids and gas molecules. Diffusion allows the number density of previously created defects to reduce, by grain growth, dislocation climb, annihilation, etc. resulting in a misfit as the film attempts to either contract or expand. However, since the in-plane misfit displacements are constrained by the attached substrate, elastic strains develop in the film. For films that deposit with a high defect density, these diffusional effects can be rapid, leading to large 'intrinsic' stresses, in the GPa range. Some of the mechanisms and the associated stresses are discussed further in the Appendix. These stresses can be either tensile or compressive. The residual stresses can also be redistributed by plastic deformation and creep [6].

In multilayers produced at high temperatures, by either co-sintering or diffusion bonding, the residual stresses derive primarily from thermal expansion misfit. The stresses are relatively uniform, with minimal gradients through the layers. Conversely, the mechanisms of 'intrinsic' stress development do not operate homogeneously as the film deposits. There is usually a change in stress with film thickness and a stress gradient within the film [6]. Typically, the first layers to deposit have the largest stress. Such behavior is generally found for inorganic films, such as oxides, nitrides, diamond, etc. Metallic films which yield upon cooling experience stress relaxation and, in consequence, are subject to a more uniform residual stress.

The residual stresses have scaling characteristics based on a reference stress, designated the *misfit stress*, σ^T , such that the actual residual stress, σ_R , can always be expressed in the form,

$$\sigma_R/\sigma^T = q \quad (2.1)$$

where q is a non-dimensional function that depends on geometry, elastic properties, etc. Several examples are presented below. In general, for the reasons indicated above, σ^T cannot be predicted from models, even when the mechanisms are known. It must be measured.

When the constituent materials and the interfaces respond to changes in temperature in an *elastic*

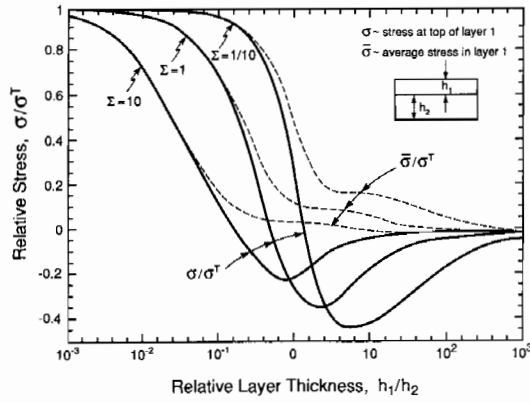


Fig. 2.3. Trend in residual stress with relative layer thickness, h_1/h_2 , for bilayers having several modulus ratios, Σ .

distance, z , from the edge ($z < L$),

$$\sigma_R(z) \approx \tau_0(z/h) \quad (2.5a)$$

or

$$\sigma_R/\sigma^T = z/L. \quad (2.5b)$$

A component normal to the interface, σ_{zz} , also exists very near the edge, as shown.

2.2.2. Bending. One important phenomenon in multilayers is bending because of the moments of stress associated with the residual field. The consequences are most vividly illustrated for an elastic *bilayer*, subject to misfit stress, σ^T defined above. Consider the geometry shown in Fig. 2.3 and let

$$\Sigma = \frac{E_1/(1-\nu_1)}{E_2/(1-\nu_2)} \quad \text{and} \quad \xi = \frac{h_1}{h_2}. \quad (2.6)$$

The average residual stress σ_R in layer #1, $\bar{\sigma}$, is related to σ^T by

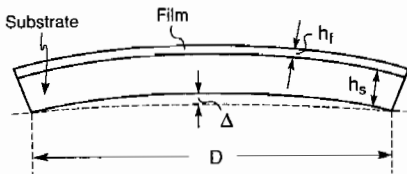
$$\bar{\sigma}/\sigma^T = \frac{1 + \Sigma\xi^3}{(\Sigma\xi^2 - 1)^2 + 4\Sigma\xi(\xi + 1)^2}. \quad (2.7a)$$

The residual stress σ at the top surface of layer #1 is

$$\sigma/\sigma^T = \frac{[1 - 3\Sigma\xi^2 - 2\Sigma\xi^3]}{(\Sigma\xi^2 - 1)^2 + 4\Sigma\xi(\xi + 1)^2}. \quad (2.7b)$$

The curvature of the bilayer caused by bending is

$$\kappa = \frac{6\xi^2(1 + \xi)}{(\Sigma\xi^2 - 1)^2 + 4\Sigma\xi(1 + \xi)^2} \left[\frac{(1 - \nu_2)\sigma^T}{E_2 h_1} \right] \quad (2.8)$$



$$\sigma_f = [E_s \Delta h_s^2] / [3(1-\nu_2) D^2 h_f]$$

Fig. 2.4. Beam deflection caused by a thin film subject to residual compression.

and the deflection δ (Fig. 2.4) is

$$\delta = -\kappa D^2/8 \quad (2.9)$$

where D is the plate diameter or length. For thin films on a thick substrate ($\xi \ll 1$), equation (2.8) reduces to [16]

$$\kappa = \frac{6h_1(1-\nu_2)\sigma^T}{E_2 h_2^2}. \quad (2.10)$$

The above results indicate that the *average* residual stress is essentially the misfit stress, σ^T , when the film is *thin* ($\xi \ll 1$), but is reduced to a fraction of σ^T when the film and substrate have comparable thicknesses, as plotted in Fig. 2.3 for three values of Σ . Bending has its maximum effect when the two layers have about equal thickness, resulting in substantial redistribution of the misfit stress. Specifically, and most importantly, the stress at the top of layer #1 develops the *opposite sign* from the misfit stress and becomes substantially larger in magnitude than the average stress in that layer, $\bar{\sigma}$ [17], as seen in Fig. 2.3. The key features brought out in Fig. 2.3 are summarized as follows: (a) When layer 1 is sufficiently thin, ($\xi \ll 1$), the residual stress in this layer is everywhere approximately the misfit stress σ^T . (b) Conversely, when layer 2 is relatively thin, ($\xi \rightarrow \infty$), the stress throughout layer 1 approaches zero. (c) Yet, in the intervening range of ξ , the stress σ at the top surface of layer #1 can have the opposite sign to σ^T and can be large compared to $\bar{\sigma}$. In particular, tensile stresses can arise at the surface of a film that would be in compression in the absence of bending. The range of ξ corresponding to such tensile stresses is of direct relevance to the crazing mode of film cracking. From equation (2.7b) it is seen that a tensile stress will exist at the top surface for all thickness ratios ξ greater than that satisfying $3\Sigma\xi^2 + 2\Sigma\xi^3 = 1$. For small Σ , the *minimum* ξ corresponds to $\xi \cong (1/2\Sigma)^{1/3}$; for $\Sigma = 1$, $\xi = 1/2$; while for large Σ , $\xi \cong (1/3\Sigma)^{1/2}$. This example for the bilayer illustrates the importance of the configurational details mentioned earlier.

2.3. Measurements methods

There are two basic approaches for determining residual stress. One approach measures the misfit stress σ^T by averaging information over a substantial area away from edges and discontinuities. Beam bending is an example. The other approach involves localized measurements of displacements in order to examine the redistributed stress. Moiré interferometry exemplifies the latter.

2.3.1. Beam deflection. The preferred approach for measuring the misfit stress is the beam deflection method [16]. This approach measures the deflection (Fig. 2.4) and infers the residual stress from equation (2.9). For systems in which the film is thin compared with the substrate, the curvature is given by equation (2.10). As discussed in connection with Fig. 2.3, σ^T can be identified with the average residual stress in the upper layer (i.e. the film) when $\xi \ll 1$. (Just how

thin the film must be for the method to be accurate can be seen in Fig. 2.3. For $\Sigma = 1$, ζ must be less than about 0.03, and for $\Sigma = 10$, ζ must be less than about 0.003.) Thus, the method can be used to measure the average residual film stress whether that stress arises from thermal expansion mismatch, or from intrinsic stresses (or combinations of the two). This remains true even when the intrinsic film stresses are nonuniform through the thickness, as long as σ^T is interpreted as the average film stress. Note that none of the properties of the film need to be known in order to measure σ^T , except its thickness. The method gives a rigorous measure of σ^T provided that $D \gg h_2$, and that the substrate is elastic. Interface decohesion from the ends would be a problem, unless the decohesion length is small.

The deflection δ needed to obtain σ^T can be measured with excellent precision by using either a laser interferometer or a mechanical profilometer. Measurement systems based on lasers have been established at many laboratories. Some are capable of continuous measurements as the temperature is varied.

Since only the average of the film stress contributes to the curvature for films which are thin compared to the substrate, stress gradients normal to the surface have no effect. Should gradients exist and be important, alternative procedures are necessary to measure them.

2.3.2. Lattice strain. Several other methods for measuring the residual stress rely on determination of the lattice strain. The strains are then converted into stresses if the elastic properties are known (not always trivial). The strains are typically determined from the

shift in intensity peaks that relate to the lattice spacings (Fig. 2.5). X-ray and neutron diffraction methods are commonly used, as well as Raman microscopy [18–20]. The strain tensor is ascertained from the shifts in either the diffraction peaks or the fluorescence. It is usually necessary to calibrate the peak shifts by imposing a known load onto the body being interrogated. In organic materials, the characteristic Raman peaks displace when a strain is imposed [19]. Such displacements can be used to measure strain with high spatial resolution ($\sim 1 \mu\text{m}$). Alternately, dopants in certain inorganic crystals give rise to fluorescence peaks when subject to laser illumination (Fig. 2.5). These peaks also displace when a strain is imposed [21]. The best known example is the Cr fluorescence peak in an Al_2O_3 host lattice [20]. This fluorescence spectroscopy approach can measure strains with a spatial resolution $< 20 \mu\text{m}$.

Beam absorption represents both an opportunity and a problem. When absorption occurs, particularly with X-rays, the measured lattice strain is a weighted average over the beam penetration depth [18], which is not precisely known. However, the penetration does depend on the beam orientation and its wavelength. The associated variations in penetration may, in principle, be used to assess gradients in stress normal to the surface.

2.3.3. Localized methods. Localized stress redistribution in thin films, multilayers and fibers can be experimentally assessed from three basic measurements. (i) *Lattice strains* can be measured by either fluorescence spectroscopy [12] or microfocus X-ray methods. (ii) *Surface displacements* can be determined by moiré interferometry or strain mapping methods [22–25] (iii) *Stresses* can be evaluated by using the thermoelastic effect [25, 26]. Some results are presented in Section 4.

3. INTERFACES

3.1. Concepts

Interfaces between dissimilar materials are susceptible to debonding and sliding. These responses need to be understood through rational models, before thin film and multilayer behavior can be predicted. There are two basically different interface responses: 'strong' and 'weak' [28]. In principle, these can be differentiated upon subjecting the interface plane to a uniform normal tensile stress. Should one of the constituent materials fail prior to interface rupture, the interface would be designated 'strong'. Conversely, should failure occur by interface separation, the interface would be considered 'weak'. However, it is not trivial to conduct such an experiment, devoid of spurious edge effects. Indirect measures are typically used to differentiate 'strong' and 'weak' interfaces.

When interfaces are 'strong', they may be susceptible to *slip* occurring in the metal within a

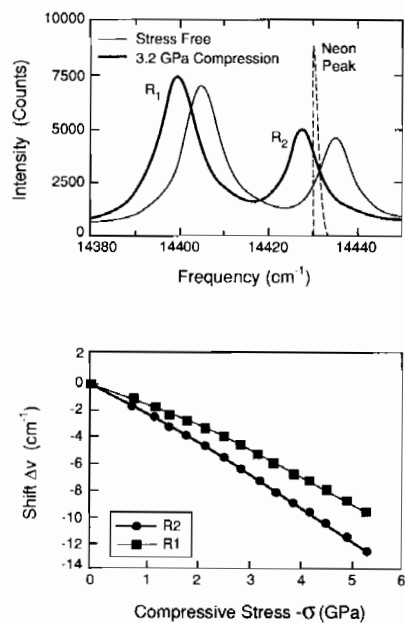


Fig. 2.5. A typical fluorescence spectroscopy measurement of the residual stress from the shift in the R_2 fluorescence peak for Cr dopants.

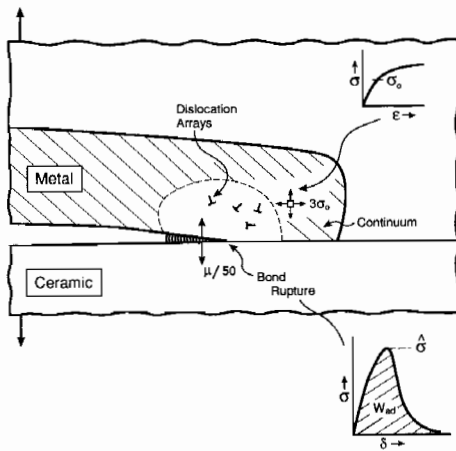


Fig. 3.1. A schematic of interface fracture by bond rupture, accompanied by plastic dissipation.

boundary layer around the interface. Such slip is an important source of stress redistribution.

'Weak' interfaces are represented by a model that allows for simultaneous fracture and deformation (Fig. 3.1). Sometimes friction is also involved [28, 29]. Fracture along the interface is characterized by a critical value of the energy release rate for the interface crack. For this purpose a mixed mode characterization of the crack tip loading is required and two special elastic mismatch parameters, called the Dundurs parameters, have a central role. For cases under consideration (each layer is isotropic), the Dundurs mismatch parameters are [7]

$$D_x = \frac{\bar{E}_1 - \bar{E}_2}{\bar{E}_1 + \bar{E}_2}$$

and

$$D_\beta = \frac{1}{2} \frac{\mu_1(1-2\nu_2) - \mu_2(1-2\nu_1)}{\mu_1(1-\nu_2) + \mu_2(1-\nu_1)} \quad (3.1)$$

where $\bar{E} = E/(1-\nu^2)$ and $\mu = E/(2(1+\nu))$. With K_I and K_{II} denoting the mode I and mode II stress intensity factors for the interface crack, the energy release rate \mathcal{G} is given by [7]

$$\mathcal{G} = \frac{1}{2} (1 - D_\beta^2) \left(\frac{1}{\bar{E}_1} + \frac{1}{\bar{E}_2} \right) (K_I^2 + K_{II}^2). \quad (3.2)$$

The phase angle ψ is used throughout this review as the measure of the relative amount of mode II to mode I loading at the interface. When $D_\beta = 0$, it is defined by [7]

$$\psi = \tan^{-1}(K_{II}/K_I). \quad (3.3)$$

When $D_\beta \neq 0$, the definition of ψ is slightly more complicated, involving a length scale [7]. The definition [equation (3.3)] suffices for the purposes of this review, since in most instances the effects of small nonzero values of D_β are minor.

The condition for a crack to advance along the interface is $\mathcal{G} = \Gamma_i(\psi)$, where Γ_i is the interfacial fracture energy measured in units of energy per unit

area. The associated decohesion energy Γ_0 represents one of the three possible contributions to Γ_i . A second contribution derives from plastic deformation, which often accompanies crack extension. A third involves friction along contacting crack faces.

The plasticity contribution is expressed through a multiplicative dissipation function \mathcal{P} [30, 31]. The most important variables are,

$$\Gamma_i = \Gamma_0 \mathcal{P}(\hat{\sigma}/\sigma_0, N, h/R_0). \quad (3.4)$$

Here, σ_0 is the uniaxial yield strength of the metal which deforms plastically, N is its strain hardening exponent, $\hat{\sigma}$ is the peak stress needed to cause interface separation (Fig. 3.1), h is the metal layer thickness and R_0 is a dimension that governs the plastic zone size, given by

$$R_0 = E\Gamma_0/3\pi(1-\nu^2)\sigma_0^2. \quad (3.5)$$

The function \mathcal{P} is discussed in Section 3.3, below.

In some cases, there is a third contribution, which occurs when the fracture surfaces come into contact behind the debond front. Such behavior is most likely when the applied loading has a substantial mode II component. Its magnitude is governed by roughness and the friction coefficient for the debonded interface [29, 32].

3.2. Measurement methods

One of the present limitations is the paucity of good measurements of the interface debond energy. Such measurements are difficult to obtain under conditions that provide controlled, stable growth of a debond crack. The major experimental problems are as follows: (i) Introducing a well-defined, debond crack at the interface. (ii) Allowing for the contribution to the energy release rate from the residual stress. (iii) The design of methods that provide measurements over a range of mode mixity relevant to practical problems. (iv) The avoidance of uncharacteristic dynamic effects that arise upon unstable crack growth.

Most of the test methods that provide satisfactory data on technologically relevant interfaces involve sandwich configurations. These must be produced by diffusion bonding at relatively high homologous temperatures and are thus restricted to certain types of interface. Moreover, there are physical size limitations on configurations that can be realistically used. In consequence, the test specimens depicted in Fig. 3.2 have been found to be most useful, because interface cracks can be extended in a stable manner, with optical monitoring of the debond [11, 28, 33]. Phase angles between $\psi = 0$ and $\sim 90^\circ$ can be accessed with these specimens.

Measurements are even more difficult for thin film interfaces produced at relatively low homologous temperatures (by sputtering, evaporation, etc.). In this case, loading the film in a controlled manner in order to evaluate \mathcal{G} at the relevant phase angle is problematic. Peel tests are widely used, but there are

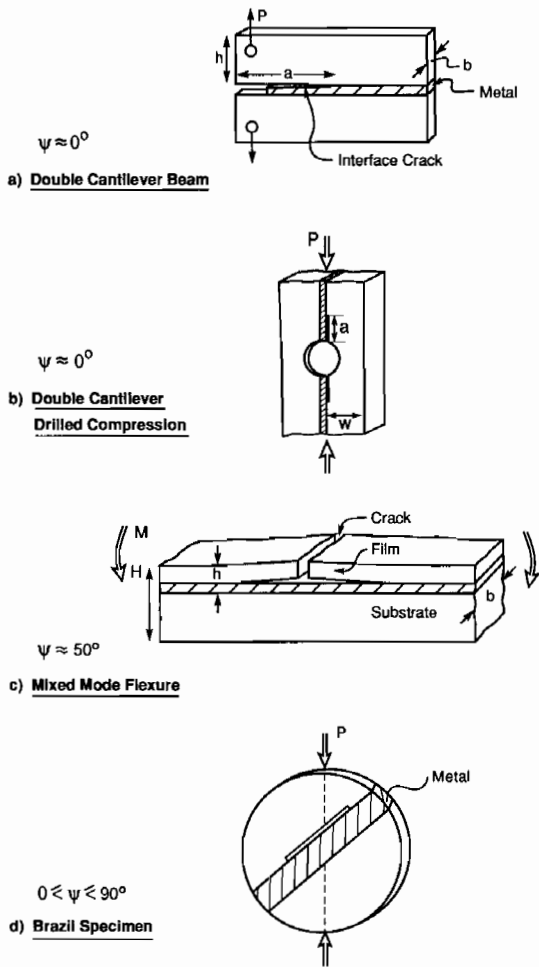


Fig. 3.2. Examples of sandwich test configurations used to evaluate the interface toughness over a range of phase angles: (b), (c) and (d) give stable crack growth.

two fundamental limitations with this test [34]. (a) It is difficult to deconvolute the force measurements to determine Γ_i . (b) The phase angle is not representative of that for typical decohesion problems [7]. Procedures in which residual stresses provide the energy release rate appear to be more satisfactory. One such method is depicted in Fig. 3.3. It uses a superposed Cr layer deposited by sputtering [35]. Such layers have a large 'intrinsic' residual tensile stress. When the layer has sufficient thickness, spontaneous decohesion occurs at the metal/ceramic interface. The critical Cr layer thickness needed for this purpose gives Γ_i . Moreover, this Γ_i is measured at phase angles, ψ between 0 and 50° , typical of those involved in many decohesion phenomena [7].

3.3. Interface separation criteria

There are several basic mechanisms of interface separation that govern Γ_0 and $\hat{\sigma}$ (Fig. 3.4). In some cases, separation occurs by plastic hole coalescence in a metal boundary layer in accordance with a ductile fracture mechanism [28] (Fig. 3.5). The stress within

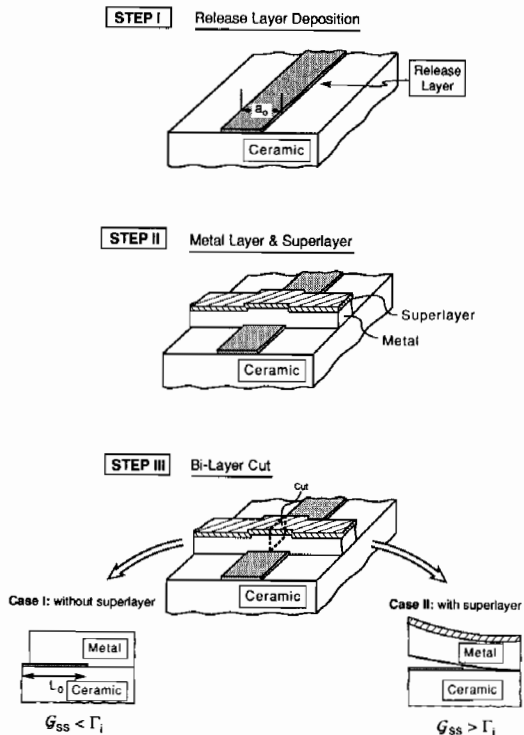


Fig. 3.3. A test method for measuring the debond energy for thin ductile films on a substrate.

the separation zone is a multiple (typically about 3) of the uniaxial yield strength of the metal, σ_0 . The separation displacement scales with the spacing l , between the hole nuclei on the interface [36], such that the decohesion energy is,

$$\Gamma_0 \approx \sigma_0 l / 2. \tag{3.6}$$

The holes usually form at a spacing related to the interface microstructure, especially the grain size [37]. Consequently, Γ_0 is microstructure sensitive and its magnitude encompasses a wide range. The lower limit, $\Gamma_0 \approx 40 \text{ Jm}^{-2}$, is exemplified by pure Al bonded to a fine grained oxide. The largest values measured

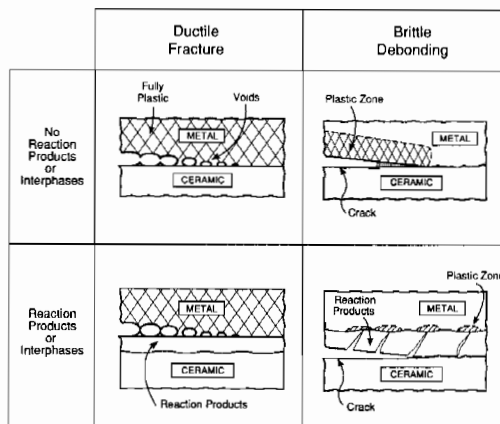


Fig. 3.4. A schematic showing mechanisms of interface failure.

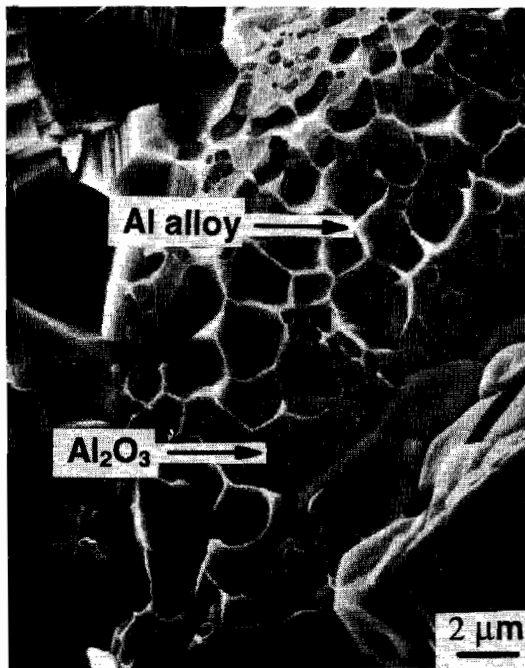


Fig. 3.5. Ductile fracture of an interface showing ridges of metal attached to the ceramic side of the debond.

without prematurely failing one of the constituents are in the range, $\Gamma_0 \approx 10^3 \text{ Jm}^{-2}$.

When *brittle interphases* or reaction products exist, decohesion often occurs *within* this phase, and the

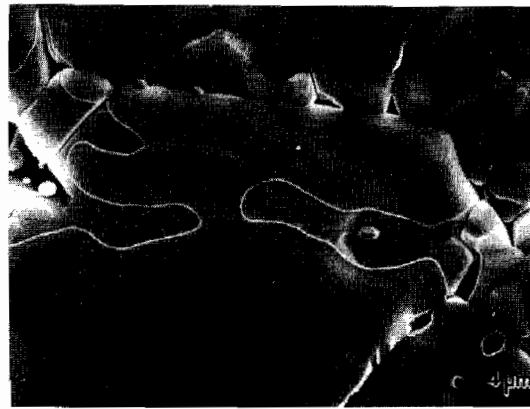
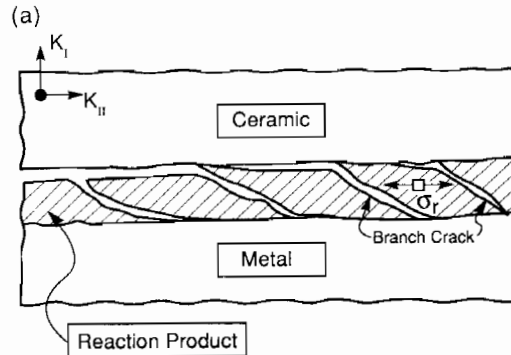


Fig. 3.6. An amorphous silicate on the Al_2O_3 side of a debond surface between Pt and Al_2O_3 . The silicate layer is outlined by the light ridge across the grain facets.

separation energy Γ_0 is related to that of the interphase itself, Γ_p [28, 38]. A practical example is the amorphous silicate phase that often exists at oxide/metal bonds (Fig. 3.6) [28, 39]. In such cases, $\Gamma_0 \approx \Gamma_p \approx 5\text{--}10 \text{ Jm}^{-2}$. There is also some dependence on the mode mixity, related to changes in crack morphology [40]. In mode I, the crack is relatively planar whereas, in mode II, *en echelon* microcracking (Fig. 3.7) is the preferred failure mechanism [38].

Brittle debonding can also occur by rupture of the bonds at the interface plane (Fig. 3.1) [41, 42]. The



(b)

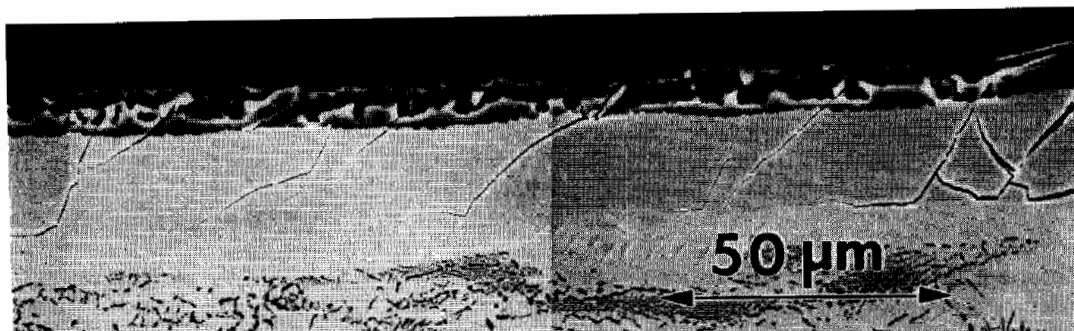


Fig. 3.7. Failure of a thin brittle layer in shear by *en echelon* microcracking: (a) schematic, (b) experimental observation for Ti/ Al_2O_3 .

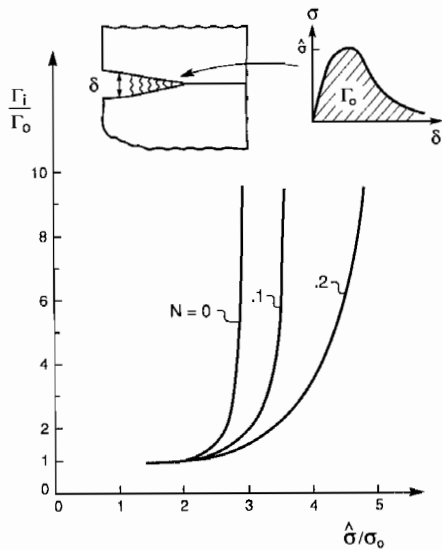


Fig. 3.8. Effects of plastic dissipation on the interface fracture energy.

equilibrium separation energy is then given by the work-of-adhesion, W_{ad} . The rupture stress $\hat{\sigma}$ is the peak value associated with the atomic separation law [44] (Fig. 3.1). This mechanism usually operates when the bond plane contains either contaminants or segregants. It is most prevalent for bonds produced at low homologous temperatures, wherein contaminants control W_{ad} and $\hat{\sigma}$ [11]. Bonds produced at higher homologous temperatures by diffusion bonding are less susceptible to contaminants, because carbon, hydrogen and oxygen typically dissolve in the metal and diffuse away from the interface. However, the segregation of impurity species to the interface may still affect W_{ad} and $\hat{\sigma}$ [42].

3.4. Plastic dissipation

The plastic dissipation is leveraged by the stress $\hat{\sigma}$ acting within the separation zone and by the separation energy Γ_0 [equation (3.4)]. It may also be affected by the layer thickness. Computations of the debond resistance have been made by assuming that each element of metal deforms in accordance with the

laws of continuum plasticity [30, 31]. The results for thick layers are summarized in Fig. 3.8 for three values of the strain hardening exponent N . The effects of layer thickness are shown on Fig. 3.9. There are three important implications:

(i) Plastic dissipation is negligible when $\hat{\sigma} < 3\sigma_0$. All of the energy is dissipated by bond separation and $\Gamma_i \approx \Gamma_0$.

(ii) When $\hat{\sigma}$ exceeds $3-5\sigma_0$ (depending on N), the plastic dissipation becomes so large in thick layers that the debond cannot propagate by interface separation. In this case, other fracture mechanisms intervene. However, when the layers become thin, $h/R_0 \geq 5$, the constraint on the plastic flow allows much larger stresses to develop. In consequence, crack growth at the interface can occur, even when $\hat{\sigma}/\sigma_0 > 5$. In this range, quite large values of Γ_i/Γ_0 can be achieved. Moreover, the scaling with layer thickness is given by

$$\Gamma_i/\Gamma_0 = (h/R_0)f(\hat{\sigma}/\sigma_0, N) + 1 \quad (3.7)$$

where f is a function that can be estimated from Fig. 3.9.

(iii) There is a major influence of the mode mixity on the plastic dissipation, even when the separation energy itself is independent of phase angle, ψ [31]. In many cases, this effect accounts for the practical difficulty found in propagating mode II debonds along interfaces.

3.5. Friction

When the interface crack is non-planar and subject to a relatively large phase angle, contacts may exist along the crack surface [29, 32]. Friction operates at these contacts, giving rise to frictional shear tractions. These tractions reduce the energy release rate at the crack tip and lead to dissipation as the debond propagates. Consequently, the debond resistance increases and is strongly influenced by the phase angle (Fig. 3.10). This frictional effect is particularly important for mode II loadings. The best known application is fiber pull-out in composites. Here, a constant friction stress τ_0 acting along the interface behind a separation zone with a designated debond

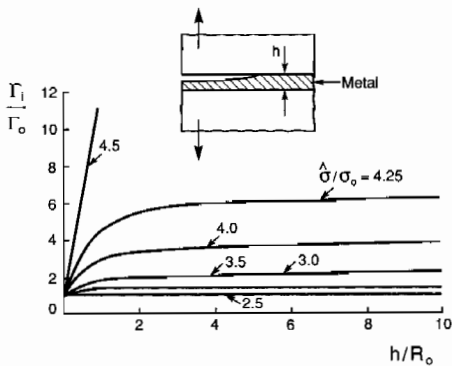


Fig. 3.9. Effects of metal layer thickness on the interface fracture energy.

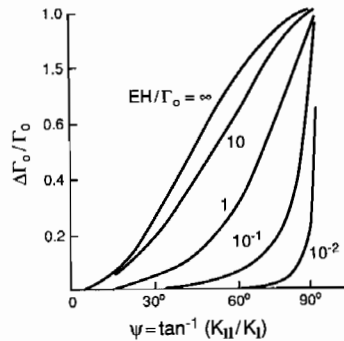


Fig. 3.10. Effect of mode mixity on the frictional contribution $\Delta\Gamma_0$ to the nominal interface fracture energy. H is the roughness amplitude.

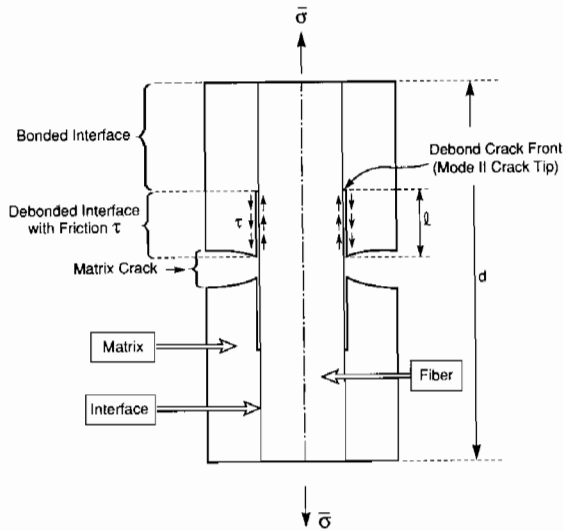


Fig. 3.11. A cell model for a fiber in a brittle matrix with a matrix crack, showing a mode II debond with frictional sliding along the debonded surfaces.

energy has been used as an acceptable representation (Fig. 3.11) [32]. Such interfaces are characterized by a combination of a mode II debond energy, Γ_1 , and a frictional sliding resistance, τ_0 .

3.6. Cyclic effects

Cracks on interfaces can propagate upon cyclic loading, even on those interfaces designated to be 'strong'. A good example is the $\text{Al}_2\text{O}_3/\text{Al}$ interface, which only ruptures by a ductile mechanism when loaded monotonically, but can debond by fatigue upon cyclic loading [11, 12]. Crack growth occurs by the same basic mechanism that operates in the mono-

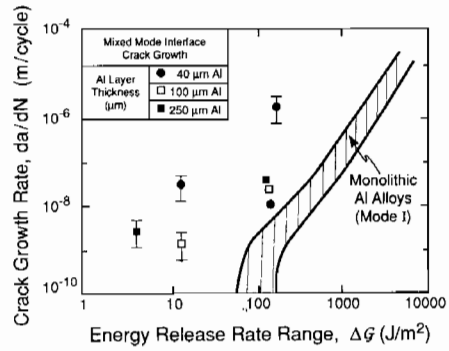


Fig. 3.13. A comparison of fatigue crack growth rates for the $\text{Al}_2\text{O}_3/\text{Al}$ interface in mixed mode ($\psi = 50^\circ$) with the mode I growth rate found for Al alloys.

lithic metal. It is accompanied by crystallographic striations on the metal side of the cyclic debond crack (Fig. 3.12). In most instances, the crack growth rates, da/dN , are somewhat larger than those found in the alloy itself, as revealed by the crack growth measurements made for $\text{Al}_2\text{O}_3/\text{Al}$ in Fig. 3.13. The larger crack growth rates probably arise because of the larger amplitude shear stress reversals that occur near the crack tip, when located at the interface [48].

There are no data for mode II fatigue crack growth along the interface, but there are indications that da/dN is appreciably less than that in mode I, as also found in the alloy itself. Such trends in mixity are similar to those found upon monotonic loading, with regard to the fracture energy, Γ_1 , as described above.

3.7. Layer thickness effects

When plastic dissipation in one of the constituents contributes to the interface fracture energy, there is

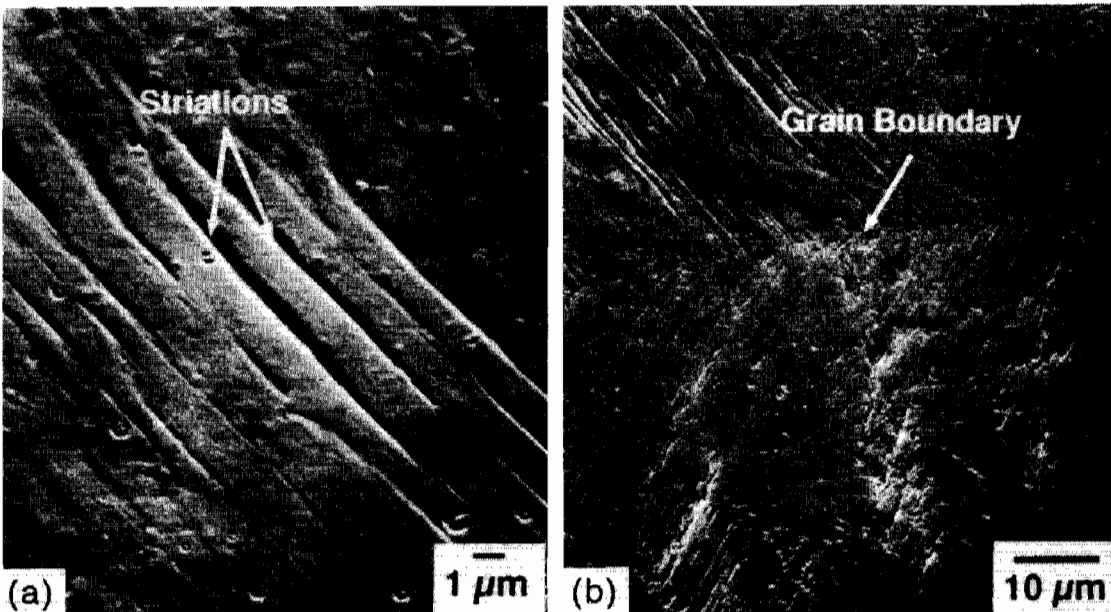


Fig. 3.12. Fatigue striations caused by an interface crack in $\text{Al}_2\text{O}_3/\text{Al}$, (a) within a single grain, (b) across a grain boundary.

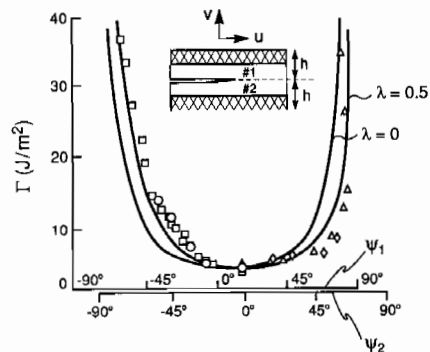


Fig. 3.14. Effects of phase angle on the interface fracture energy for epoxy/glass interfaces. (See Ref. [7] for the choice of ψ .)

an influence of layer thickness on Γ_i , given by equation (3.7). This situation arises for either thin films or multilayers, when their thickness, h , is smaller than the plastic zone width, R_0 . In this case, the plastic zone is limited by the layer width and the plastic dissipation diminishes as h reduces [31, 41, 49]. The trend in Γ_i with h depends on the mode mixity, as well as differing for thin films and embedded thin layers, because of the different constraints on plastic flow. Predictions have been obtained for a sandwich system loaded in mode I (Fig. 3.9) by using continuum plasticity to represent the deformation in the ductile layer [49]. When the layer is sufficiently thin compared to R_0 , most of the plastic dissipation is eliminated and Γ_i approaches Γ_0 . Once the layer thickness exceeds the size of the plastic zone (which is larger than R_0 for $\hat{\sigma}/\sigma_0 > 3$), no further increase in Γ_i occurs.

3.8. Fracture energy measurements

The most complete sets of data are those for an epoxy/glass interface (Fig. 3.14) obtained using a specially designed specimen and loading device [43]. These data demonstrate the strong influence of mode mixity on Γ_i . In this case, plastic dissipation in the epoxy dictates $\Gamma_i(\psi)$ [43]. Unfortunately, this loading device could not be used for metal/ceramic bi-material systems, which have significantly larger

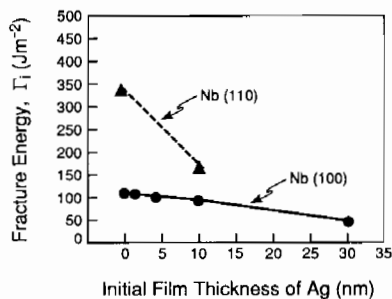


Fig. 3.15. Effects of Ag segregation on fracture energy for the $\text{Al}_2\text{O}_3/\text{Nb}$ system for two Nb orientations (110) and (100).

elastic moduli. Consequently, the results for metal/ceramic interfaces do not encompass a complete range of variables. Most of these data are for Al_2O_3 bonded to various metals at relatively high homologous temperatures. For 'strong' interfaces, a ductile fracture mechanism operates, particularly when Al and Cu are used. In tests performed on these interfaces, plastic hole growth and coalescence in the metal near the interface leaves ridges of metal on the oxide fracture surface [28, 37] (Fig. 3.5). These findings are qualitatively consistent with the prediction (Fig. 3.8) that brittle interface crack cannot occur when $\hat{\sigma}/\sigma_0$ is large. Instead, holes are generated at the interface, leading to a debond energy given by equation (3.6). These interfaces have a sufficiently large Γ_i that fracture often proceeds preferentially in the oxide [40].

For 'weak' systems, the interface between the metal and the oxide can physically separate, with metal exclusively on one debond surface and oxide on the other [41, 42]. For these interfaces, the values of Γ_i measured range between $\sim 4 \text{ Jm}^{-2}$ for $\text{Al}_2\text{O}_3/\text{Mo}$ [44] and $> 10^3 \text{ Jm}^{-2}$ for $\text{Al}_2\text{O}_3/\text{Nb}$ [45]. There is evidence indicating effects on Γ_i of stress corrosion, segregation, strain-rate, phase angle and metal layer thickness. Resistance curve behaviour also exists [41], involving plastic dissipation. A rigorous explanation for the occurrence of decohesion by bond rupture at these interfaces, rather than hole growth, has yet to be provided. The segregation of impurities near the interface, which influences local plasticity and the bond separation stress, $\hat{\sigma}$, is probably important.

Two sets of data are briefly examined: one for $\text{Al}_2\text{O}_3/\text{Ag}/\text{Nb}$ [42] and the other for $\text{Al}_2\text{O}_3/\text{C}/\text{Au}$ [41]. The study of Ag segregation to the $\text{Al}_2\text{O}_3/\text{Nb}$ interface (Fig. 3.15) has shown that the fracture energy can be substantially affected by segregants. There are also effects of the Nb orientation, which affects the plasticity. Such behavior is qualitatively consistent with equation (3.4).

In the $\text{Al}_2\text{O}_3/\text{Au}$ system, effects of metal layer thickness on Γ_i have been found [41], as anticipated by equation (3.4). However, the estimate of $\hat{\sigma}/\sigma_0$ obtained from Fig. 3.9 is relatively small, $\hat{\sigma}/\sigma_0 \approx 4.5$, inferring an unrealistically low bond strength, $\hat{\sigma} \approx 600 \text{ MPa}$ [46]. In this system, C segregates to the interface, and reduces the bond strength, but probably not to such low levels. Moreover, plasticity occurring at the submicron scale in the vicinity of the debond tip probably causes the local stresses to substantially exceed those predicted by the continuum model [28]. The significance of this effect can be appreciated from calculations that simulate interface crack growth by interposing a thin elastic layer between the debond and the plastic zone [47] (Fig. 3.16). The implication is that Γ_i/Γ_0 can be of order 10^2 or larger, with considerable plastic dissipation, while still allowing crack growth by bond rupture at the interface.

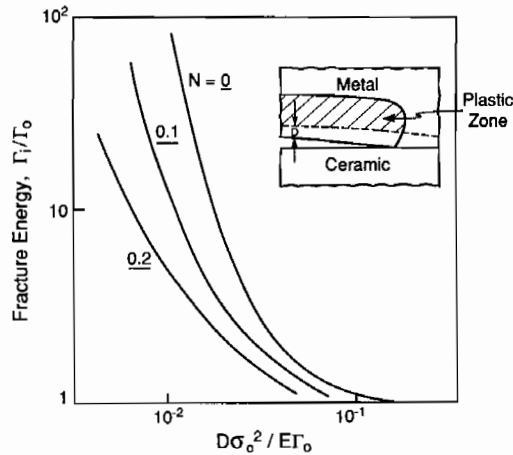


Fig. 3.16. Effect of the elastic layer thickness D on the plastic dissipation that accompanies interface crack growth by bond rupture.

4. CRACKING AND DECOHESION

4.1. Mechanics concepts: steady-state cracking

The basic mechanics needed to predict the onset of either interface debonds or cracks in the ceramic have been established [7]. The limitation has been poor quality data, particularly on the interface properties and the plastic flow resistance of thin layers. A fundamental discovery from the mechanics is that many of the cracking and decohesion problems in stressed multilayer structures are subject to a steady-state energy release rate, \mathcal{G}_{ss} . When this energy release rate is equated to the relevant fracture energy, a lower bound condition for cracking is found. This condition is associated with a critical layer thickness, h_c having non-dimensional form [7, 50].

$$E\Gamma/h_c(\sigma^T)^2 = \lambda \tag{4.1}$$

where λ is a configuration dependent, non-dimensional cracking number (of order unity) and Γ is the relevant fracture energy (ceramic or interface). The significance of this result is appreciated upon noting that, when $h < h_c$, there is insufficient strain energy to propagate a crack or debond to any appreciable distance. It thus represents a fail-safe condition. It has particular significance for systems that require high reliability. The incidence of cracking and decohesion when $h > h_c$ is probabilistic in nature and dependent on manufacturing defects. Some fundamental solutions for the cracking number are illustrated in Fig. 4.1. For surface cracking and channeling (also called craze cracking), the relevant toughness Γ in (4.1) is the film toughness, provided that there is no debonding at the interface. For debonding, it is the interface toughness Γ_i (at $\psi \approx 50^\circ$). For spalling, Γ is the mode I substrate toughness. The substrate damage mode involves both the film and the substrate toughnesses.

These solutions rely on two fundamental mechanics problems: (i) *Decoctions* or cracks that

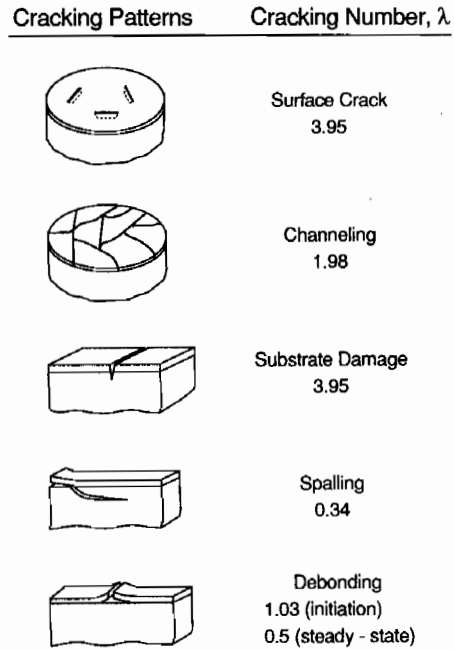


Fig. 4.1. Some fundamental cracking and decohesion problems, indicating magnitudes of the cracking number, λ .

originate from edges and propagate either along or parallel to the interfaces, and (ii) Cracks normal to the plane of the film or layer which originate from interior or edge flaws and propagate across the film or layer. Selected results on these two problems applicable to steady-state behavior are presented.

4.1.1. *Decohesion and spalling.* Decoctions along the interface, and spalling cracks propagating parallel to the interface, derive their energy release rate from the changes in stresses ahead and behind the crack tip (Fig. 4.2). Steady-state conditions are attained once the crack has extended a distance from the left edge in Fig. 4.2 equal to several times the smaller of either h or H . In steady-state, the energy-release can be obtained by a relatively elementary analysis accounting for the difference in elastic energy stored well ahead and well behind the crack tip. By equating \mathcal{G}_{ss} to Γ at the appropriate ψ , solutions to most of the important decohesion and substrate cracking problems have been derived. The phase angle ψ characterizing the mode mix requires a more complicated analysis, but complete numerical results are now available [7].

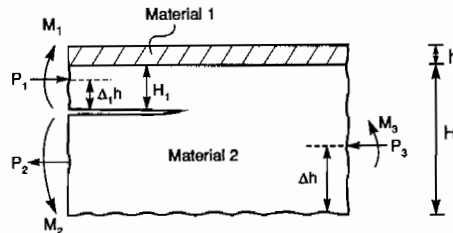


Fig. 4.2 A schematic showing forces P and moments M created by residual stress or external loading in a bilayer.

The steady-state solution for the geometry and loadings shown in Fig. 4.2 permits the solution to a wide variety of cases. In a given application, the magnitudes and signs of the load and moment quantities (each defined per unit thickness perpendicular to the plane of the figure), P_i and M_i , are calculated from stress distributions in the layers in a manner illustrated for a number of examples in Ref. [7]. The energy-release rate is given by:†

$$2\bar{E}_2\mathcal{G}_{ss} = \frac{P_1^2}{hA_1} + \frac{M_1^2}{h^3I_1} + \frac{P_2^2}{h(\xi - \xi_1)} + \frac{12M_2^2}{h^3(\xi - \xi_1)^3} - \frac{P_3^2}{hA} - \frac{M_3^2}{h^3I} \quad (4.2)$$

where the loads and moments (per unit thickness) are defined on Fig. 4.2, $\xi = H/h$, $\xi_1 = H_1/h$ and now $\Sigma = \bar{E}_1/\bar{E}_2 = (1 + D_\alpha)/(1 - D_\alpha)$ with $\bar{E} \equiv E/(1 - \nu^2)$

$$A = \xi + \Sigma$$

$$I = \Sigma[(\Delta - \xi)^2 - (\Delta - \xi) + 1/3] + \Delta\xi(\Delta - \xi) + \xi^3/3$$

$$\Delta = \frac{\xi^2 + 2\Sigma\xi + \Sigma}{2(\xi + \Sigma)}$$

A_1 , I_1 and Δ_1 have the same definitions, but with ξ replaced by ξ_1 and Δ replaced by Δ_1 . The expression for the energy-release rate holds whether the crack is on or off the interface.

If the crack is off the interface, as depicted in Fig. 4.2, the mode mixity is given by

$$\tan \psi = \frac{\sin \omega - (M/hP)\sqrt{U/V} \cos(\omega + \gamma)}{\cos \omega + (M/hP)\sqrt{U/V} \sin(\omega + \gamma)} \quad (4.3)$$

where

$$P = P_1 - C_1P_3 - C_2M_3/h$$

$$M = M_1 - C_3M_3$$

with

$$C_1 = A_1/A, \quad C_3 = I_1/I$$

$$C_2 = (A_1/I)[\xi - \Delta] - (\xi_1 - \Delta_1).$$

The geometric factors are

$$1/U = 1/A_1 + 1/(\xi - \xi_1) + 12 \frac{[\Delta_1 + (\xi - \xi_1)/2]^2}{(\xi - \xi_1)^3}$$

$$1/V = 1/I_1 + 12/(\xi - \xi_1)^3$$

$$\sin \gamma / \sqrt{UV} = 12 \frac{[\Delta_1 + (\xi - \xi_1)/2]}{(\xi - \xi_1)^3}.$$

The only quantity not specified by these formulae is ω . It is an angle, tabulated in Ref. [51], having a weak

†The notation of Ref. [7] is retained in equations (4.2) and (4.3). Note that the definition of ξ in these equations differs from its use earlier in the paper. The expressions for Δ and Δ_1 given here correct misprints in those in Ref. [7].

dependence on ξ , ξ_1 and the moduli mismatch parameters D_α and D_β . For no modulus mismatch and for deep substrates, $\omega \approx 52^\circ$. The above expression for ψ holds without modification when the crack lies on the interface provided that there is no elastic mismatch. With mismatch, whenever D_β can be neglected, the only modification is that the quantity ω has a small jump from its value for a crack just below the interface (depending on D_α). Values of ω for the interface crack are given in Ref. [7]. When D_β is not insignificant, there is a slightly more complicated interpretation of ψ [7].

4.1.2. Layer cracking. Cracks that form *within* thin brittle layers, extend normal to the principal tensile stress and interact with the interfaces. The interaction leads to *tunneling* or *channeling* modes of crack extension (Fig. 4.3). These modes also have a steady-state energy release rate which can be obtained from the solution to the two-dimensional plane strain problem for the cracked layer well behind the propagating crack front (Fig. 4.3). Let \mathcal{G}_{ss} be the energy-release rate averaged over the tunneling crack front. An energy balance accounting for the release of energy per unit advance of the crack front under steady-state conditions gives $2h\mathcal{G}_{ss}$. It is the work done by the tractions acting across the plane of the layer crack, in the plane strain problem, as those tractions are reduced to zero. With σ denoting the stress in the layer prior to cracking and δ as the average crack opening displacement ($2h\delta = \int_0^{2h} \delta \, dx$), the steady-state energy-release rate of the tunneling crack is

$$\mathcal{G}_{ss} = \int_0^\sigma \delta(\bar{\sigma}) \, d\bar{\sigma}. \quad (4.4)$$

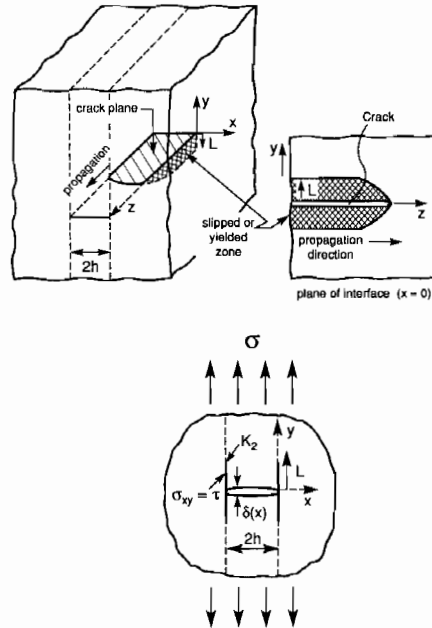


Fig. 4.3. A schematic of crack growth by tunnelling with slip or debonding at the interface.

The fundamental result for a crack tunneling through a layer of thickness $2h$ is

$$\mathcal{G}_{ss} = \frac{\pi(1 - \nu^2)\sigma^2 h}{2E} f(D_\alpha, D_\beta) \quad (4.5)$$

where E and ν pertain to the layer. If there is no elastic mismatch between the layer and the adjoining layers the function, $f=1$. Otherwise, it depends somewhat on the elastic mismatch parameters [51–53]. This result also assumes that no debonding, sliding or plastic yielding occurs where the crack intersects the neighboring layers. Either sliding or yielding along the interface, as depicted in Fig. 4.3, increase the average opening displacement of the crack and thereby increase the steady-state energy release rate [14]. Equation (4.5) also applies to channeling, or crazing, cracks in a thin film of thickness h . Then $f=1.258$ in the absence of both elastic mismatch and interface relaxation [52, 53].

4.1.3. Crack path. A decision to be made concerns the preference for either interface debonding or ceramic cracking. To facilitate this decision, steady-state cracks are first assumed to exist either in the ceramic or at the interface. The crack within the ceramic is located on a plane having a zero mode II stress intensity factor ($K_{II} = 0$), because this is the preferred crack trajectory in brittle materials. The energy release rates are then sequentially calculated and compared with the corresponding fracture energies. The mode I value is used for the ceramic, Γ_c . For the interface, the debond energy Γ_i must be specified at the appropriate phase angle, ψ , which must be calculated. Alternately, the choice of trajectory is determined by whether a pre-existing interface crack prefers to continue along the interface or *kink* into the ceramic [7, 54]. For this purpose, the relative energy release rates for continued extension of the debond

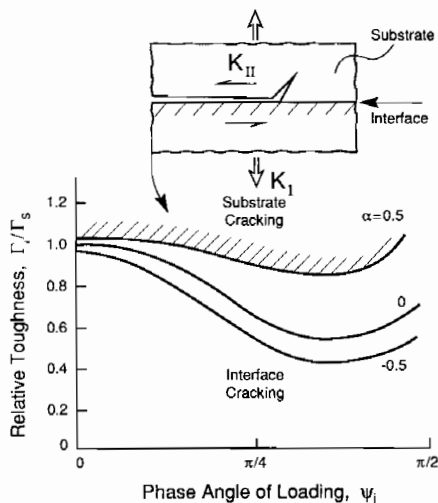


Fig. 4.4. A kinking diagram indicating conditions that either give interface crack growth or cause cracking of the ceramic.

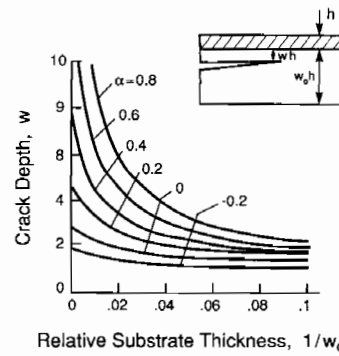


Fig. 4.5. The predicted crack plane ($K_{II} = 0$) in the substrate for films in residual tension on a brittle substrate.

and for a kink into the ceramic provide the basic mechanics. As expected, there is a strong influence of the loading-phase ψ . The decision about the preferred crack path is made by equating the energy release rates to the respective fracture energies, resulting in a kinking diagram (Fig. 4.4).

When the crack does not extend along the interface, but instead, propagates into the ceramic, the crack path is determined exclusively by the criterion, $K_{II} = 0$ [7]. When the brittle layers are in *compression*, such paths exist *parallel* to the interfaces, at a characteristic distance from the interface [7]. An important feature of the mechanics is the appreciable configuration dependence. Namely, results for thin layers on semi-infinite substrates become inapplicable at a surprisingly large value of the substrate thickness (Fig. 4.5). This aspect of the solutions arises because bending of the material both above and below the decohesion plane has a considerable influence on both the energy release rate and the mode mixity. This bending reduces \mathcal{G}_{ss} , because it limits the strain energy available for crack growth. It also, usually, reduces ψ , by inducing a larger opening at the crack faces. Consequently, while the solutions for semi-infinite substrates provide the necessary insight about decohesion and delamination (as well as the correct order), rigorous fail-safe predictions for actual configurations require additional analysis.

4.2. Mechanics concepts: stress redistribution

When cracks tunnel through one of the brittle layers, simultaneous slip or debonding at the interface can increase the steady-state energy release rate, as discussed above, and thereby lower the resistance of that layer to cracking. However, these same effects reduce the stress concentration in adjacent layers, suppressing the spread of cracks out of a given layer. These other mechanisms of stress redistribution must be considered in the design of effective multilayers.

Before examining the stress solutions, it is useful to relate the extent of either slip or debonding to the constituent properties. There are two ranges governed by the ratio of the slip length, L , to the half-crack size, h . When L/h is small (e.g. ≤ 0.5), a

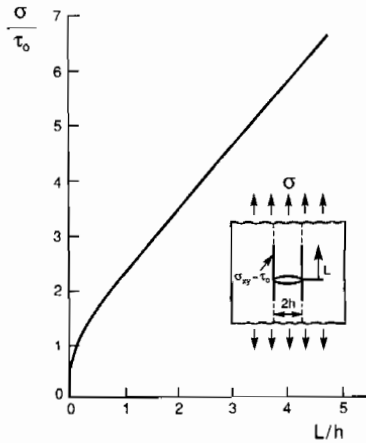


Fig. 4.6. The variation in slip length with applied stress showing the small-scale yielding and shear lag regimes.

small-scale yielding (SSY) results applies [14]:

$$L/H = 0.052\pi[\sigma^T/\tau_0]^2 \quad (4.6)$$

where σ^T is considered to be uniform and τ_0 is the shear resistance of the slipping material. When L/h is large (≥ 1), numerical analysis gives [14] (Fig. 4.6),

$$L/h \approx [\sigma^T/\tau_0] - 1. \quad (4.7)$$

This result differs slightly from the analytical solution [equation (2.4)].

Two basic stress solutions provide the key insights. (i) The asymptotic near tip solution for a semi-infinite crack impinging on an interface (Fig. 4.7). (ii) The full-field solution for a cracked layer designated the H-crack problem (Fig. 4.8).

The asymptotic problem [14] (i) is applicable when the extent of debonding or slipping is small compared to the length of the crack itself. Let K denote the stress intensity factor of the crack in the absence of either debonding or slipping. It plays the role of the load. Solutions for the stress ahead of the crack are plotted in Fig. 4.7 for two cases: (1) with debonding extending a distance d along the interface on either side of the main crack and (2) with slip along the interface

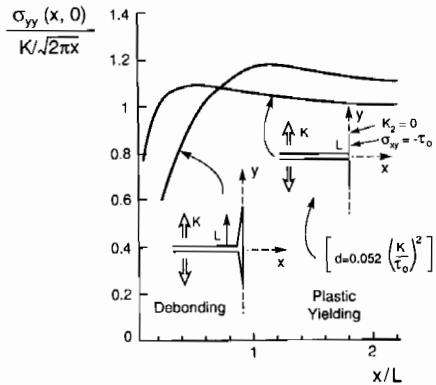


Fig. 4.7. Asymptotic solution for stress redistribution by slip and debonding from a crack tip, as a function of slip/debond length.

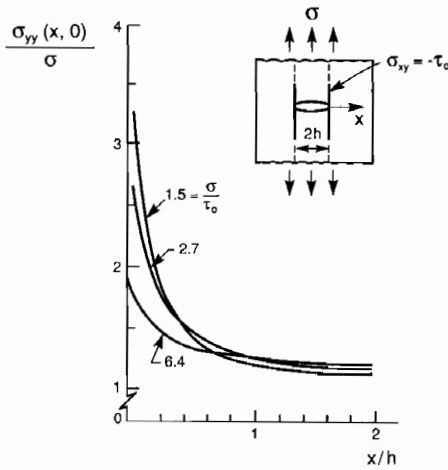


Fig. 4.8. Full-field solutions for stress redistribution around an embedded crack, by slip, for various shear resistances.

governed by a critical shear stress τ_0 acting on the interface. In case (1), the interface crack is open and thus frictional effects are not expected to come into play. Case (2) models slip due to plastic yielding of a vanishingly thin ductile adhesive layer along the interface. The interface remains closed and the distance over which slipping occurs is given by equation (4.6). The normal stress acting on the plane ahead of the main crack tip is plotted in Fig. 4.7. It is normalized by the elastic solution in the absence of either debonding or slip (i.e. by $K/\sqrt{2\pi x}$). The abscissa in this figure is the distance from the interface x normalized by the debonding or slipping distance L . Thus, values of the ordinate less than unity represent stress levels which have been reduced by sliding or slip. Note that debonding is more effective than yielding in redistributing the stress ahead of the crack.

Full-field solutions (ii) for the embedded crack extending across a layer (Fig. 4.8) are valid when the sliding or slip zones extend above the crack by distances comparable or greater than the thickness of the layer itself. These results exhibit some of the same basic features seen above and provide additional detail suitable for comparison with experimental measurements. One feature which does change involves the debonding interface. For this case, the interface crack is *closed* when the debond zone length L exceeds roughly $(1/4)h$. The solutions are thus similar to those for *slip*, with τ_0 becoming the friction stress, τ_s . The consequence is that debonding is not necessarily such an effective means of stress redistribution.

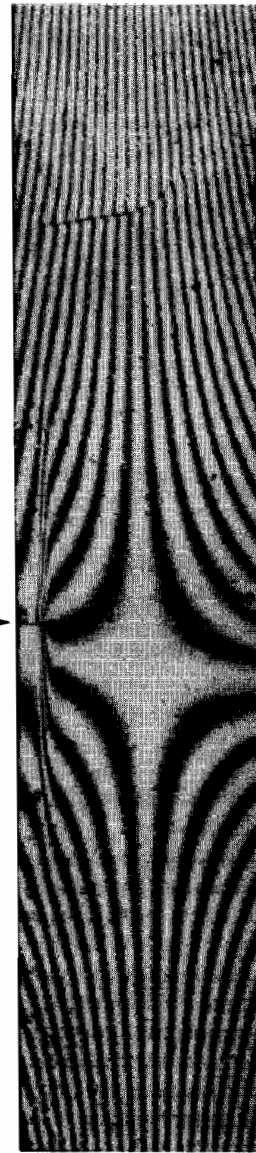
A different situation arises when a *surface crack* exists in the outermost layer, an example of which is shown in Fig. 4.9. The debonds generated from the crack are mixed mode ($\psi \approx 50^\circ$), such that the cracked interface is open and the crack tip attains a steady-state energy release rate (\mathcal{G} independent of interface crack length under constant bending moment) for L greater than several times h_1 . The

debond can thus extend without limit, whenever the energy release rate reaches the mixed-mode interface toughness, Γ_i . Such debonding evidently eliminates stress concentrations at the point where the layer crack first meets the interface [12]. However, should the debond arrest because the loading is not pure bending, there are stress concentrations near the debond tip, associated with the magnitude of Γ_i .

4.3. Experimental measurements

Experimental measurements on multilayers have been made using the $\text{Al}_2\text{O}_3/\text{Al}$ and $\text{Al}_2\text{O}_3/\text{Cu}$ systems, subject to imposed plus residual stresses [12, 25]. These systems, which have 'strong' interfaces upon monotonic loading, may be used to assess the effects of slip on stress redistribution. For this purpose, surface cracks have been introduced into the outermost Al_2O_3 layer and the system loaded in four-point flexure. The moiré interferometry and fluorescence spectroscopy methods have been used to probe the displacements and lattice strains, respectively. The extent of slip is best visualized by moiré interferometry after loading and unloading (Fig. 4.10). The residual displacements caused by slip in the metal boundary layer are then readily discerned. The extent of slip is completely consistent with analysis (Fig. 4.11).

While under load, moiré interferometry can also be used to obtain displacement measurements at high spatial resolution [25] ($\sim 1 \mu\text{m}$). A typical result is shown in Fig. 4.12. Strains in the Al_2O_3 layers are obtained directly from the displacement vectors. A comparison of measured strains with those calculated for 'H-cracks' subject to uniform tensile loading, at the corresponding L/a (Fig. 4.8) indicate good correspondence. Moreover, it is noted that the strains are quite closely represented by the solution for an elastically homogeneous, isotropic body, even though there has been considerable slip in the Al [25].



Pre-crack →

Fig. 4.10. A moiré interferometry image of the slip band formed in $\text{Al}_2\text{O}_3/\text{Al}$ multilayers. The band initiates at the precrack tip and spreads vertically.

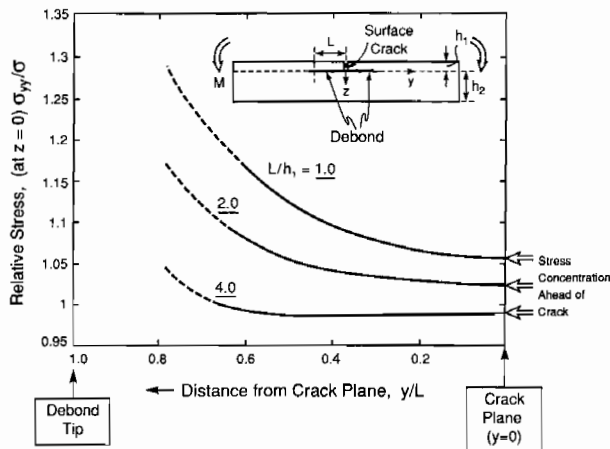


Fig. 4.9. A surface crack illustrating mixed-mode debonding. Also shown are the stresses when the multilayer is in bending.

Fluorescence spectroscopy measurements confirm this behaviour [12] (Fig. 4.13). The important conclusion, as noted earlier, is that the slip lengths have to be considerable before there is an appreciable reduction in the stress concentration around a crack.

When the same interfaces are debonded by cyclic loading (to a distance, $L/a \approx 2$), Fig. 4.14, the stress concentration, measured by fluorescence spectroscopy, is eliminated [12] (Fig. 4.13). As already noted, debonding from a surface crack is mixed mode, such that relief of the normal stresses occurs, causing a substantial reduction in the stress concentration. The measured stresses are consistent with those calculated for a multilayer in bending with a debonded interface [12] (Fig. 4.9).

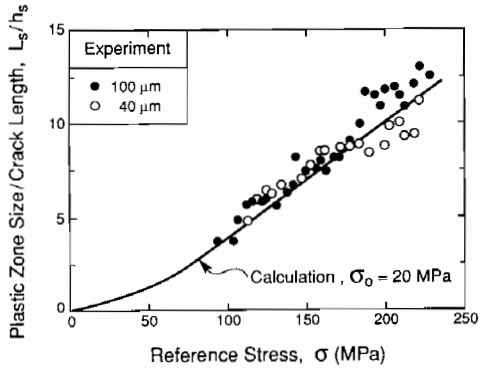


Fig. 4.11. A comparison of plastic zone size measurements for Al/Al₂O₃ multilayers with calculations for a shear yield strength, $\tau_0 = 20$ MPa.

4.4. Fail-safe design concepts

In multilayer systems with at least one brittle layer, there are three competing modes of thermo-mechanical damage: (i) tunnel cracking or crazing,

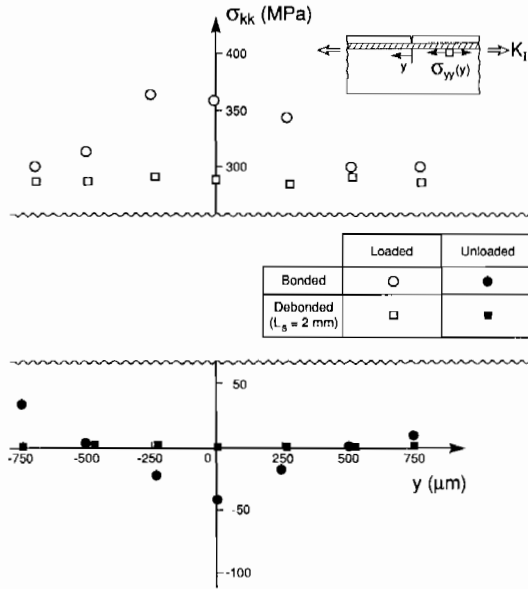


Fig. 4.13. Fluorescence spectroscopy measurements of σ_{kk} stress around a surface crack in Al₂O₃/Al multilayers for a strongly bonded, slipping interface and an interface debonded by fatigue.

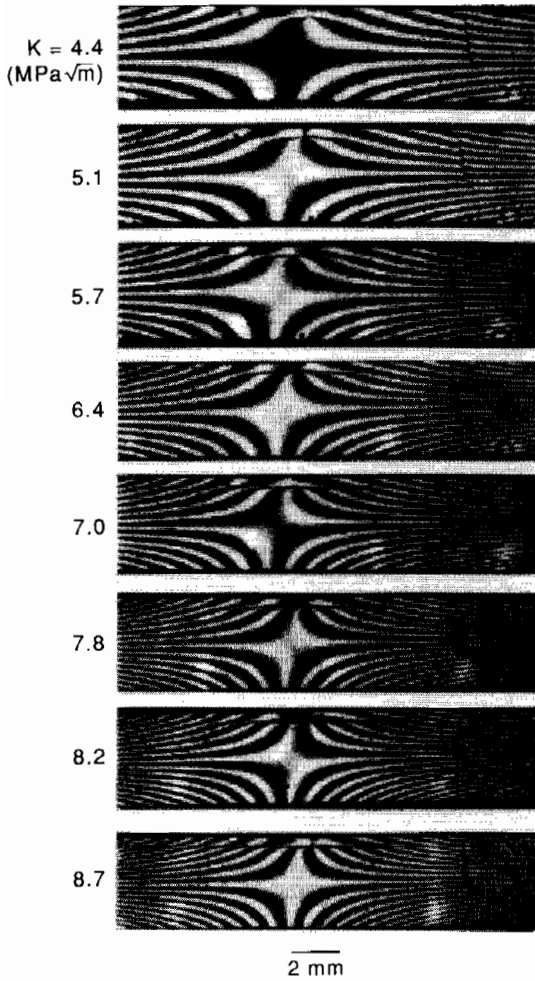


Fig. 4.12. Moiré interferometry images of displacements around a surface crack in Al₂O₃/Al multilayers at eight different values of the nominal stress intensity factor, K . The precrack is at the top in the center.

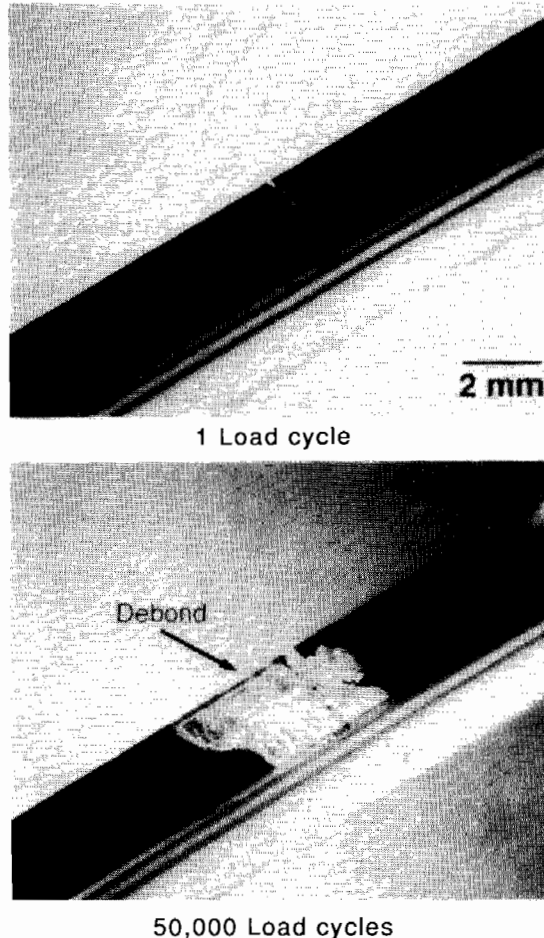


Fig. 4.14. Optical image of a debond created by fatigue in an Al₂O₃/Al multilayer.

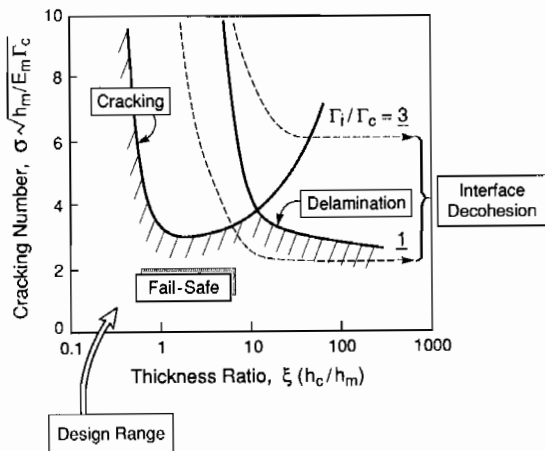


Fig. 4.15. A fail-safe diagram for a bilayer, reflecting the three brittle damage modes.

(ii) spalling or delamination, (iii) interface decohesion. A fail-safe concept ensures that *none* of these three damage modes may operate. The concept can be illustrated for a *bilayer*, following a scheme first proposed by Spearing *et al.* [17]. One of the layers is metallic, designated *m*, and the other is a brittle material, designated *c*.

Fail-safe conditions arise upon considering the steady-state solutions for each of the three brittle damage modes (Fig. 4.15). *Delamination* and interface decohesion reflect the steady-state behavior represented by equation (4.1), but involving different values of Γ and λ . The results can be plotted in space represented by the cracking number and Γ_i/Γ_c , with Γ_c being the fracture energy for the brittle material. The delamination behavior involves a determination of the location of the crack in the brittle layer, using Fig. 4.5, which, in turn, influences the magnitude of λ . When the brittle substrate is not thin compared to the metal layer, there is no mode I path located within the brittle material. In this range, delamination is not a viable damage mode. However, interface decohesion is still possible, in mixed mode, whenever Γ_i is relatively small.

Crazing of the brittle film has a steady-state governed by channeling, again given by equations (4.4) or (4.5) such that the same space can be used to represent the craze susceptibility. A conservative solution for channel crack growth is obtained by assuming that the tensile stress in the brittle layer is uniform and given by σ at the top of the film [equation (2.7b)]. The incidence of crazing then reflects the influence of thickness ratio on σ . A less conservative solution can be generated by accounting for the stress gradient by using equation (4.4).

Fail-safe behavior is represented by the lower *envelope* of the three failure modes. It is sensitive to the ratio, Γ_i/Γ_c (Fig. 4.15). However, it is only necessary that $\Gamma_i/\Gamma_c \gtrsim 1$ to ensure that interface decohesion does not limit integrity. At larger values of Γ_i , delamination and crazing of the brittle

layers are the limiting damage modes. Crazing is most relevant at small relative thicknesses ($\xi \lesssim 10$), whereas delamination limits integrity at larger thicknesses.

4.5. Damage modes

The manner in which damage may progress across a multilayer is strongly dependent on the redistribution of stress by slip or decohesion at the interface discussed in Section 4.2. A particularly important distinction occurs when a crack already exists in one of the brittle layers. This crack may extend in a coplanar manner into the next brittle layer, leading to the formation of a dominant crack with essentially brittle behavior when externally loaded. Alternatively, other cracks may form elsewhere in other brittle layers, in a strictly stochastic manner. This latter *damage* behavior results in inelastic strains and structurally superior performance. This distinction is analogous to a well-known phenomenon found in fiber composites, referred to as either global load sharing (GLS) (distributed fiber damage) or local load sharing (LLS) (dominant crack) [55, 56]. The transition between GLS and LLS is clearly related to the stresses in layers adjacent to the layer containing the crack. However, a criterion for further cracking is also needed. This criterion has been based on probabilistic aspects of the tensile strengths of the brittle layers, subject to the stress distribution that occurs in the layers around the crack. However, there are no definitive probabilistic solutions, because of the complexity of re-evaluating the stress distribution as each crack forms within a stochastic simulation.

When conditions exist that result in distributed damage, GLS analysis relates the ultimate tensile strength (UTS) of a loaded multilayer to the constituent properties of the layers. The key feature is that the gauge length relevant to the stochastic analysis becomes $\sim 2L$ [equation (4.7)] such that the layers have a characteristic strength S_c . This behavior arises because cracks separated by distances $\gtrsim 2L$ do not have interacting stress fields. A consequent scaling relationship for the UTS, designated S_u , is [56]

$$S_u \sim f S_0 [\tau L_0 / h S_0]^{1/(m+1)} \quad (4.8)$$

where m is the shape factor, f the volume fraction of brittle layers, S_0 the scale factor in the layer strength distribution and L_0 is a reference length.

Local load sharing conditions that result in the growth of a dominant crack lead to behavior governed by the stresses in the intact layer ahead of the crack. By equating the peak tensile stress to the characteristic layer strength, S_c , a renucleation stress intensity factor, K_N , can be obtained [25]. For example, when there are no ligaments present and slip is the preferred interface response, the elastic solution still applies in the range, $L/a \gtrsim 5$; then,

$$K_N \approx S_c \sqrt{2\pi h} \quad (4.9)$$

where h is the layer half-thickness. At larger slip lengths, K_N increases. Moreover, as the crack extends and ligaments develop, the crack growth resistance, K_R , increases. Some typical experimental results [31] demonstrating these behaviors are summarized in Fig. 4.16. Note that thick layers enhance both K_R and K_N . However, special thin layer effects can arise in the submicron range, which may cause reversions in behavior as h reduces.

4.6. Some practical problems

When multilayers consisting of several different materials are designed to be fail-safe against decohesion and delamination, initially a simple procedure is needed to establish the most likely decohesion site and the associated steady-state energy release rate. For this purpose, it is recalled that cracking of one of the brittle constituents parallel to the interface occurs on a plane having $K_{II} \approx 0$. An analysis for locating this plane in an arbitrary multilayer represents the first important requirement. Then \mathcal{G}_{SS} on that plane is needed for comparison with the fracture energy of the brittle material, Γ_c . Simultaneously, it is necessary to evaluate \mathcal{G}_{SS} and the associated mode mixity at each of the interfaces. These must be compared with $\Gamma_i(\psi)$.

It is important to appreciate that the solutions are configuration dependent, because of the strong influence of bending on both \mathcal{G}_{SS} and ψ . As emphasized before, analytical results for semi-infinite

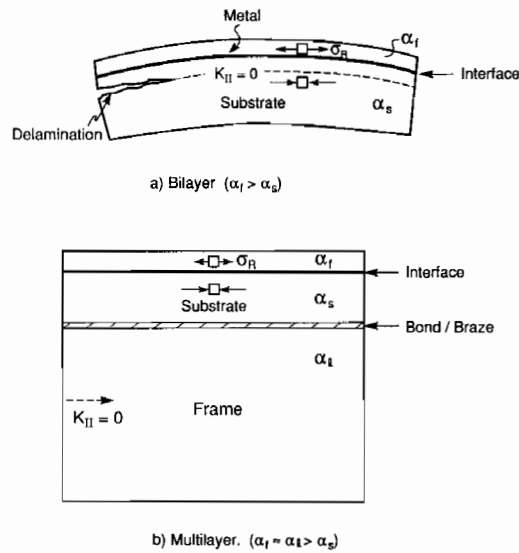


Fig. 4.17. A schematic showing the configuration dependence of delamination cracking in a multilayer.

substrates can, therefore, be misleading. Experimental results may indicate the absence of decohesion and delamination in one configuration. Yet, another configuration made from the same materials may be prone to these phenomena, and vice versa. The design of experiments to validate fail-safe systems requires careful analysis to ensure that the appropriate values of \mathcal{G}_{SS} and ψ actually obtain at the most failure-prone layers and interfaces. An example is given in Fig. 4.17 for a metal/ceramic system, in which the interface is 'strong'. As a bilayer, a $K_{II} = 0$ plane exists in the ceramic parallel to the interface, as indicated on Fig. 4.5. The associated energy release can cause the ceramic to delaminate, whenever $\mathcal{G}_{SS} > \Gamma_c$. Such behavior is found in the Cu/AlN system, when the Cu exceeds a critical thickness. However, ceramic failure is not inevitable. It can be suppressed if the bilayer is bonded or brazed to a metallic substrate having the appropriate thermal expansion coefficient. In particular, if the substrate has essentially the same thermal expansion coefficient as Cu and a high yield strength, the $K_{II} = 0$ plane is displaced into the substrate. A crack that begins in the AlN will thus deviate into the bond plane rather than propagate in the ceramic parallel to the interface. The system will thus sustain thermostructural integrity provided that the bond to the substrate is itself 'strong'.

5. THERMOMECHANICAL FATIGUE

Various cyclic effects can operate in thin films and multilayer systems, because of the dissimilar thermo-physical properties of the constituents. These are thermal and mechanical in nature. They cause changes in stress and may introduce damage, which eventually leads to failure. All of these phenomena are embedded in the fundamentals of cyclic plastic deformation, occurring at various physical scales. It

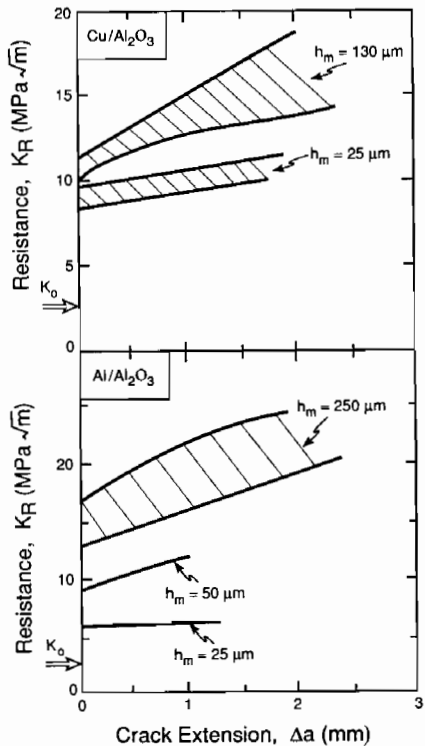


Fig. 4.16. Resistance behaviors found in two layered materials.

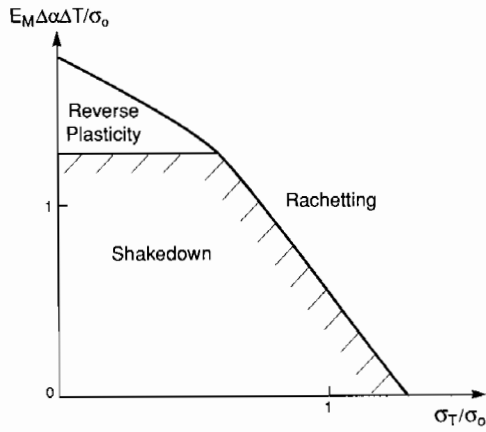


Fig. 5.1. A thermal fatigue diagram for a multilayer.

is convenient to separately address the phenomena that occur with and without cracks being present.

Before cracks form in the film or multilayer, thermal cycling may modify the residual stresses and can cause either damage or ratchetting. A thermal fatigue diagram [10] (Fig. 5.1) indicates the ranges in which these phenomena occur, when a transverse stress is also applied to the system. When this stress, σ_T , is fixed as the temperature cycles, by ΔT , the

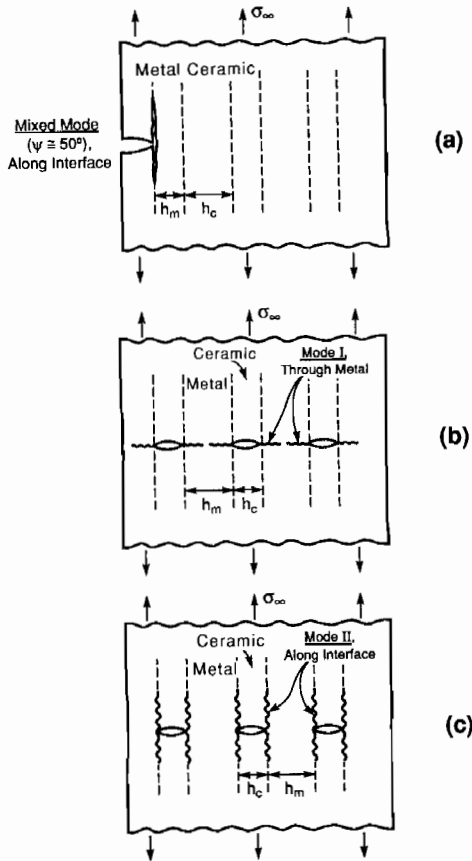


Fig. 5.2. A schematic comparing fatigue debonding at the interface with cyclic crack growth through the alloy.

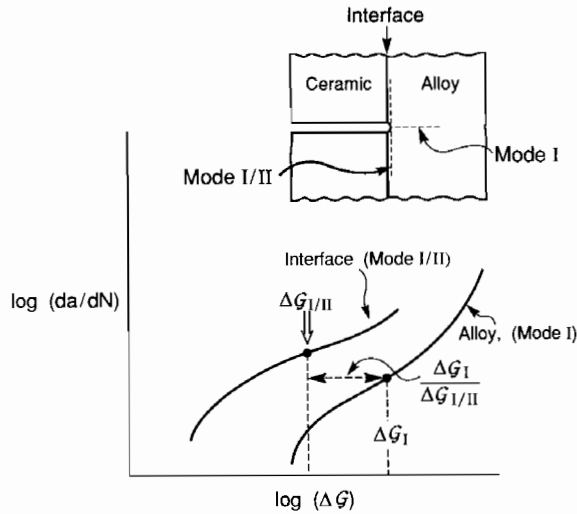


Fig. 5.3. A schematic illustrating the criterion governing the fatigue crack trajectory.

shakedown range is [10]

$$\sigma_T / \sigma_s + \Delta T / \Delta T_s = 1 \quad (5.1)$$

where $\sigma_s = 1.3 \sigma_0$. Within a range bounded by ΔT_s and σ_0 , *shakedown* occurs. In this range, the stresses adjust to a new level, as thermal cycling proceeds, such that all subsequent behavior is *elastic*. Thereafter, the system is dimensionally stable and the stresses are predictable. Outside this range, various detrimental phenomena arise. With predominantly thermal loading, the plastic deformation that occurs with each cycle typically leads to cracking and interface debonding. When *transverse* loads are also present, ratchetting may occur, whereby plastic strain accumulates with each thermal cycle. The strain per cycle then increases as either ΔT or σ increase above the shakedown threshold values ΔT_s and σ_s .

When cracks begin to form in the brittle layers, additional fatigue effects arise. The cracks may either extend by fatigue into the metal, in mode I, or debond the interface (Fig. 5.2) [11, 12]. The choice depends upon two ratios: the energy release rate range, $\Delta \mathcal{G}$ and the crack growth rates, da/dN , at the relevant

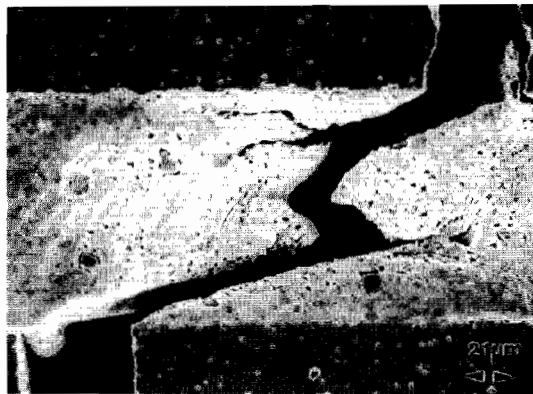


Fig. 5.4. Fatigue failure of a bridging alloy ligament.

mode mixity. For a *surface crack*, debonds are mixed mode ($\psi \approx 50^\circ$), as already discussed. The *mixed-mode* interface da/dN should be compared with the *mode I* growth rate in the alloy (Fig. 3.13), at the relevant $\Delta\mathcal{G}$. The energy release rate for interface growth is less than that for growth into the alloy, by a factor ranging between 4 (initial) and 2π (steady state) [7]. If the interface growth rate is larger than the alloy growth rate, at this reduced $\Delta\mathcal{G}$ (Fig. 5.3), then cyclic interface debonding is preferred, and vice versa. For $\text{Al}_2\text{O}_3/\text{Al}$ multilayers, it is found that debonding from a surface crack occurs in preference to crack growth through the alloy [12] (Fig. 5.3), consistent with the larger da/dN at the interface.

The converse behavior obtains when a long crack is present, bridged by intact metal ligaments [12] (Fig. 5.4). Then, mode I fatigue cracking of the alloy occurs in preference to interface debonding. For this case, the energy release rate ratio is essentially the same as that for the surface crack [7]. However, the debond growth rate along the interface is lower, because it is subject to mode II loading, with accompanying frictional resistance. The preference is thus for growth of a fatigue crack through the alloy, causing rupture of the ligaments [12, 57]. An embedded crack is expected to behave in a similar manner, but there have been no experimental measurements.

6. THIN LAYER EFFECTS

When the films or layers have submicron thickness, some special thin layer effects arise. One is related to the *threading* of dislocations through the ductile material. Another is governed by the elevation of the *tunnel cracking* resistance.

The threading of a dislocation through a thin layer occurs at a critical stress σ_c (Fig. 6.1) inversely dependent on the layer thickness, h , in accordance with the non-dimensional formula [8]

$$\sigma_c h / G_r b = \chi \quad (6.1)$$

where G is the shear modulus and b is the Burgers' vector, with χ being a threading number. For a thin film with an oxide layer on the surface, χ is given by

$$\chi = \frac{\tan \phi}{2\pi(1-\nu)\cos \theta} \left[\frac{G_s}{(G_r + G_s)} \ln \left(\frac{2.6h}{b} \right) + \frac{G_0}{(G_r + G_0)} \ln \left(\frac{17.5h_0}{b} \right) \right] \quad (6.2)$$

with G_0 being the shear modulus of the oxide layer and h_0 its thickness, while ϕ and θ are the angles that define the slip plane and slip direction, respectively, within the film. The threading predictions are consistent with the flow strengths measured for metal films having sufficiently small thickness that σ_c exceeds the bulk yield strength, σ_0 [8]. This thickness is typically, $h \approx 0.1\text{--}1 \mu\text{m}$. At larger thicknesses, the bulk behavior applies, subject to the equivalent microstructure.

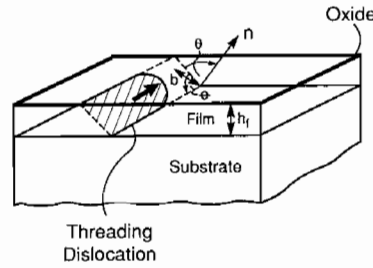


Fig. 6.1. A schematic of a threading dislocation in a thin film with an oxide layer.

Namely, grain size effects must be included, through the Hall-Petch effect [8].

A comparison of the dislocation threading result with the tunnel cracking formula relevant to the brittle layer [equation (4.1)] provides some useful insight. Upon equating the threading strength [equation (7.1)] to the tunnel cracking resistance [equation (4.1)], a critical thickness, h_* , is derived as

$$h_* = \left(\frac{Eb^2}{\Gamma} \right) \frac{\chi^2}{4\lambda(1+\nu)^2}. \quad (6.3)$$

At layer thickness $h > h_*$, dislocation threading occurs more readily than cracking and vice versa. This result suggests a tendency toward more brittle behavior as the layer thickness decreases.

7. DESIGN METHODOLOGY

The preferred design methodology would (i) use the minimum number of experiments needed to determine the relevant constituent properties and residual stresses and (ii) provide a software program that identifies the most likely sites of delamination and cracking, as well as computing the associated energy release rates and mode mixities. Most applications are for either thin layers generated by vapor deposition or thick layers formed by post firing or co-sintering. These are often attached to other systems, either by subsequent adhesive bonding or brazing. Frequently, electroplated layers are also present. The residual stresses and the fracture energies need to be measured, preferably, on the actual multilayers, following each of the major steps in the fabrication cycle. In some cases, the elastic properties also need to be determined, because the films contain porosity, particularly along columnar grain boundaries in vapor deposited material.

Residual stress measurements on either vapor deposited thin films or sintered thick films are most reliably achieved by simultaneously applying the same film to a *reference substrate*, within the same fabrication run. Then, either beam bending or fluorescence spectroscopy measurements can be made on the reference system. In some cases, these measurements can be made on standard substrates, such as Si and sapphire, in order to obtain the reference temperature, T_R , as well as the shakedown range ΔT_S when yielding occurs. Such measurements

often provide enough information to calculate the residual stresses expected when other substrates and multilayers are used. For this purpose, it is necessary to use the reference tests to (i) evaluate the 'lock-in' temperature for films fabricated at high temperature (but otherwise are elastic), (ii) obtain the strength profile $\sigma_0(T)$ for films that yield on cooling (Fig. 2.1), (iii) determine creep relaxation rates $\sigma^{-1}(T, \dot{T})$ for films that experience high homologous temperature subsequent to their fabrication.

Interface fracture energies can be influenced by each thermal cycle in the fabrication sequence, because of segregation and interdiffusional effects. Γ_i should be measured either on the actual multilayer or on representative thin layers subjected to thermal cycles that simulate the fabrication sequence. The preferred approach is to deposit a thick superlayer of either Cr or Cu onto the layer of interest, until the critical thickness that causes spontaneous decohesion is reached [35]. If the brittle material is found to delaminate, the interface is considered to be 'strong' enough and explicit measurements of Γ_i are not necessary.† Otherwise, the procedure described in Section 3 (Fig. 3.2) may be used to explicitly evaluate Γ_i (at $\psi \approx 50^\circ$). When a superlayer sufficiently thick to achieve delamination cannot be vapor deposited, a layer may be added by brazing, provided that the braze has been adequately characterized. Each interface can be assessed in this manner. In cases where Γ_i is needed at very different mode mixities, superstructures can be designed to give smaller values of ψ at the interface.

This overview has summarized existing knowledge about the thermomechanical characteristics of multilayers. Some areas have benefited from appreciable recent progress, such as the mechanics of cracking and decohesion. Other areas have only been dealt with in a superficial manner. Critical areas for future endeavors concern the details of the thermomechanical response, leading to fail-safe design codes. Also there is still much to be learned about interface debonding, particularly the interplay between segregation and the plastic flow properties of the metal in thin layers.

REFERENCES

1. IBM J. Res. Dev. **36**, 817 (1992).
2. S. Winzer, N. Shanker and A. P. Ritter, *J. Am. Ceram. Soc.* **21**, 2246 (1989).
3. G. W. Goward, *Proc. Workshop on Coatings for Advanced Heat Engines*, NTIS, Springfield, Va (July 1987).
4. *J. Hard Mater.* **2**, 3 (1991).
5. A. T. English and C. M. Melliar-Smith, *A. Rev. Mater. Sci.* **8**, 459 (1978).
6. M. F. Doerner and W. D. Nix, *CRC Crit. Rev. Solid States Mater. Sci.* **14**, 224 (1988).
7. J. W. Hutchinson and Z. Suo, *Adv. Appl. Mech.* **29**, 63 (1992).
8. W. D. Nix, *Metall. Trans.* **20A**, 2217 (1989).
9. C. H. Hsueh and A. G. Evans, *J. Am. Ceram. Soc.* **68**, 120 (1985).
10. S. Jansson and F. A. Leckie, *J. Mech. Phys. Solids* **40**, 593 (1992).
11. R. M. Cannon, B. J. Dalgleish, R. K. Dauskhart, T. S. Oh and R. O. Ritchie, *Acta metall. mater.* **39**, 2145 (1991).
12. M. C. Shaw, M. Y. He, B. J. Dalgleish, D. B. Marshall and A. G. Evans, *Acta metall. mater.* **42**, 4091 (1994).
13. S. Suresh, *Fatigue of Materials*. Cambridge Univ. Press (1991).
14. K. S. Chan, M. Y. He and J. W. Hutchinson, *Mater. Sci. Engng.* **A167**, 57 (1993).
15. H. C. Cao and A. G. Evans, *Acta metall. mater.* **39**, 2997 (1991).
16. D. S. Campbell, *Handbook of Thin Film Technologies*. McGraw-Hill, New York (1970).
17. S. M. Spearing, M. A. Tenhover, D. B. Lucko, L. Viswenathan and D. K. Hollen, MRS Publication. In press.
18. M. Murakami, T. S. Kuan and I. A. Bleck, *Treatise Mater. Sci. Technol.* **24**, 163 (1982).
19. R. J. Young, R. J. Day, M. Zakakhini and I. M. Robinson, *Comp. Sci. Technol.* **34**, 243 (1989).
20. Q. Ma and D. R. Clarke, *J. Am. Ceram. Soc.* **76**, 1433 (1993).
21. L. Grabner, *J. Appl. Phys.* **49**, 580 (1978).
22. D. R. Williams, D. L. Davidson and J. Lankford, *Engng Mech.* **20**, 4 (1980).
23. M. S. Dadkhah, F. X. Wang and A. S. Kobayashi, *Engng Technol.* **7**, 28 (1988).
24. M. R. James, W. L. Morris and B. N. Cox, *Exp. Mech.* **30**, 60 (1990).
25. M. C. Shaw, D. B. Marshall, M. S. Dadkhah and A. G. Evans, *Acta metall. mater.* **41**, 3311 (1993).
26. N. Harwood and W. M. Cummings, *Thermoelastic Stress Analysis*. Adam Hilger, IOP (1991).
27. A. K. Wong, J. G. Sparrow and S. A. Dunn, *J. Phys. Chem. Solids* **49**, 395 (1988).
28. A. G. Evans and B. J. Dalgleish, *Acta metall. mater.* **40**, 5295 (1992).
29. A. G. Evans and J. W. Hutchinson, *Acta metall.* **37**, 909 (1989).
30. V. Tvergaard and J. W. Hutchinson, *J. Mech. Phys. Solids* **40**, 1377 (1992).
31. V. Tvergaard and J. W. Hutchinson, *J. Mech. Phys. Solids* **41**, 1119 (1993).
32. J. W. Hutchinson and H. Jensen, *Mech. Mater.* **9**, 139 (1990).
33. P. G. Charalambides, J. Lund, A. G. Evans and R. M. McMeeking, *J. Appl. Mech.* **101**, 77 (1989).
34. N. Aravas and K. S. Kim, *Int. J. Solids Structures* **24**, 417 (1988).
35. A. Bagchi, G. E. Lucas, Z. Suo and A. G. Evans, *J. Mater. Res.* **9**, 1734 (1994).
36. A. G. Varias, Z. Suo and C. F. Shih, *J. Mech. Phys. Solids* **40**, 485 (1992).
37. B. D. Flinn, C. S. Lo, F. W. Zok and A. G. Evans, *J. Am. Ceram. Soc.* **73**, 369 (1993).
38. A. Barlett and A. G. Evans, *Acta metall. mater.* **41**, 497 (1993).
39. M. De Graef, B. J. Dalgleish, M. R. Turner and A. G. Evans, *Acta metall. mater.* **40**, 5333 (1992).
40. R. M. Cannon, R. O. Ritchie and B. J. Dalgleish, *Acta metall. mater.* Accepted for publication.
41. I. E. Reimanis, B. J. Dalgleish and A. G. Evans, *Acta metall. mater.* **39**, 3133 (1991).

†When substrate delamination occurs rather than interface decohesion, this method may be used to obtain the mode I fracture energy of the substrate when other data are unavailable.

42. D. Korn, G. Elssner, H. F. Fischmeister and M. Rühle, *Acta metall. mater.* **40**, S355 (1992).
43. K. M. Liechti and Y. S. Chai, *J. Appl. Mech.* **59**, 295 (1992).
44. M. R. Turner, J. B. Davis, J. P. A. Löfvander and A. G. Evans, *Acta metall. mater.* Accepted for publication.
45. N. P. O'Dowd, C. F. Shih and M. G. Stout, *Int. J. Solids Structures* **29**, 571 (1992).
46. J. R. Smith, H. Schlosser and J. Ferrante, *Metal/Ceramic Interfaces* (edited by M. Rühle *et al.*) Pergamon Press, Oxford (1989).
47. Z. Suo, C. F. Shih and A. G. Varias, *Acta metall. mater.* **41**, 1551 (1993).
48. C. Woeltjen, C. F. Shih and S. Suresh, *Acta metall. mater.* **41**, 2317 (1993).
49. V. Tvergaard and J. W. Hutchinson, *Phil. Mag.* **70**, 641 (1994).
50. A. G. Evans, M. S. Hu and M. D. Drory, *J. Mater. Res.* **3**, 1043 (1988).
51. Z. Suo and J. W. Hutchinson, *Int. J. Solids Structures* **25**, 1337 (1989).
52. J. L. Beuth, *Int. J. Solids Structures* **29**, 155 (1992).
53. T. Ye, Z. Suo and A. G. Evans, *Int. J. Solids Structures* **29**, 2639 (1992).
54. M. Y. He and J. W. Hutchinson, *J. Appl. Mech.* **56**, 270 (1989).
55. M. Y. He, A. G. Evans and W. A. Curtin, *Acta metall. mater.* **41**, 871 (1993).
56. W. A. Curtin, *J. Am. Ceram. Soc.* **74**, 2837 (1991).
57. K. T. Rao, G. R. Odette and R. O. Ritchie, *Acta metall. mater.* **40**, 353 (1992).

APPENDIX

Intrinsic Stresses in Vapor Deposited Films

When a vapor-deposited polycrystalline film is grown on a substrate having an incoherent interface, there is no obvious mechanism for generating stress in the surface layer as it deposits. Surface diffusion allows atom displacements which relax strains as they attempt to develop. This situation differs from that for coherent, single crystal films which incur coherency strains.

Intrinsic stresses usually develop as a consequence of subsequent diffusional effects that occur in previously deposited sections of the film [6]. This involves mechanisms which eliminate those defects present in the film which have an associated 'free volume'. The one exception concerns the stresses associated with surfaces and interfaces, discussed below.

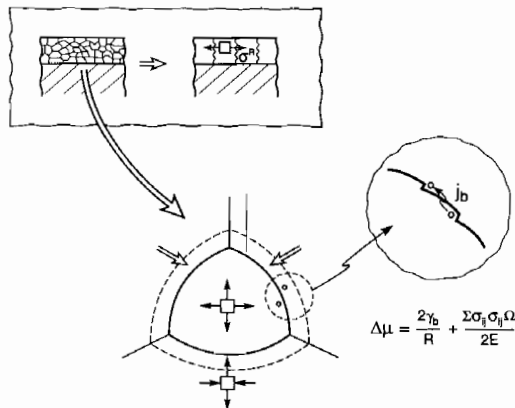


Fig. A1. A schematic of the potentials that cause grain growth and the consequent residual tensile stress in the film.

Vapor deposited films typically have a thin, equiaxed polycrystalline layer close to the interface. Above this layer, a columnar grain structure develops with a preferred crystallographic orientation. A common experience is that the equiaxed layer has a higher residual stress than the columnar material [6], resulting in bending when the film is removed from the substrate.

Intrinsic stresses in films are generally in the range 0.5–4 GPa. They can be tensile or compressive. They are also superposed on thermal expansion mismatch stresses. The mechanisms to be considered emphasize phenomena capable of giving GPa level stresses. Furthermore, the defects that give rise to the stresses, as they are eliminated by diffusion, must have sufficient density to provide the misfit strain, ϵ_T , which governs the intrinsic stress, σ_1 , through the relation

$$\sigma_1 = E\epsilon^T/(1 - \nu). \quad (\text{A1})$$

MECHANISMS

A1. Grain growth

The grain boundary is a source of 'free-volume' that diminishes as the grains grow, *subsequent to deposition*. As a small grain disappears (Fig. A1), stresses develop [6]. These stresses provide a strain energy contribution to the chemical potential of the atoms on the two sides of a grain boundary. The transformation strain ϵ^T associated with the process (depicted in Fig. A1) is,

$$\epsilon^T = 6\left(\frac{1}{d} - \frac{1}{d_0}\right)\Delta a \quad (\text{A2})$$

where d is the actual grain size, d_0 is the initial value as the film deposits, Δa is the grain boundary free volume per unit area (which is of order the atomic dimension). The contribution of the strain energy to the chemical potential difference is

$$\Delta\mu_s = \frac{1}{2}E\Omega(\epsilon^T)^2 \quad (\text{A3})$$

where Ω is the atomic volume and E is Young's modulus. This potential adds to that from the grain boundary curvature, given by

$$\Delta\mu_b = (2\gamma_b/d)\Omega \quad (\text{A4})$$

where γ_b is the grain boundary energy.

By setting the potential difference to zero, there is an equilibrium residual stress, σ_{eq}^R , which occurs at an equilibrium grain size, d_{eq} . Of course, the temperature needs to be large enough to allow grain boundary diffusion at a sufficiently rapid rate to attain this equilibrium. The equilibrium values are obtained by equating $\Delta\mu_s$ and $\Delta\mu_b$ to give

$$\sigma_{eq}^R = 3\gamma_b/2(\Delta a) \quad (\text{A5a})$$

and

$$d_{eq} = \frac{3(1 - \nu)d_0^2\gamma_b}{4E(\Delta a)^2}. \quad (\text{A5b})$$

Note that these stresses develop with time at temperature, by *grain boundary diffusion*. Moreover, the stresses *cannot* be eliminated by heat treatment. Higher stresses are more likely in fine grained material, which has a higher initial motivation for grain growth. *Only tensile stresses* arise.

For this mechanism to apply to vapor deposited films, it would be necessary for the initial grains that form during deposition to be quite small and then grow into the classical columnar configurations found when deposition is complete. The misfit strain required to achieve the equilibrium strain is of order, $\epsilon \approx 5 \times 10^{-3}$. Such strains can be achieved by removing at least one grain boundary from each $\sim 0.5 \mu\text{m}$ of film. The initial grains would need to be of order $0.2 \mu\text{m}$ or less and grow to twice their initial size as deposition proceeds.

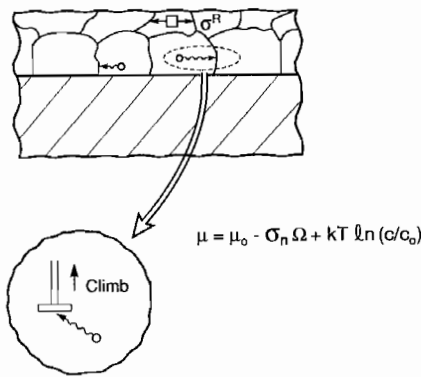


Fig. A2. The potential for point defect annihilation at edge dislocations leading to climb.

A2. point defect annihilation

If point defects are trapped in the film as it grows, they have a 'free volume'. Their subsequent elimination at either grain boundaries or dislocations must cause 'intrinsic' stress [6]. The annihilation of vacancies or interstitials is well-simulated by analysis of dislocation climb (Fig. A2). The chemical potentials in the system are given by

$$\mu = \sigma_n \Omega + kT \ln C/C_0 + \mu_0 \tag{A6}$$

where C/C_0 is the excess point defect concentration, μ_0 is the reference potential, and σ is the stress normal to the dislocation. There is an equilibrium 'intrinsic' stress which obtains when, $\mu - \mu_0 = 0$. It is given by,

$$\sigma_{eq}^R = \left(\frac{kT}{\Omega} \right) \ln(C/C_0). \tag{A7}$$

For example, if the excess defect concentration, $C/C_0 \approx 2$,

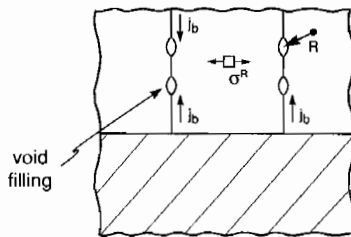


Fig. A3. Fluxes involved in the removal of voids at the grain boundaries by sintering.

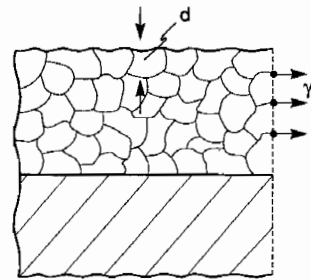


Fig. A4. The grain boundary stresses in the thin film.

then $\sigma_{eq}^R \approx 2$ GPa. This stress again develops with time at temperature. It requires lattice diffusion and thus occurs slowly. Once present, the stresses cannot be eliminated. Instead, they may increase upon annealing. These stresses can be either tensile (vacancies) or compressive (interstitials). There is no obvious grain size effect on the stress. However, the stresses develop more rapidly in small grained films, because the diffusion distances are smaller.

In order to develop equilibrium level intrinsic stresses, misfit strains of $\sim 10^{-3}$ must be possible. This represents a high defect supersaturation, which should be detectable by experiment.

A3. Sintering

Voids present on the grain boundaries upon deposition can be eliminated by subsequent sintering to create a residual tensile stress (Fig. A3). This stress has a maximum value given by the radius of curvature R of the as-deposited voids,

$$\sigma_{eq}^R = 2\gamma_s/R \tag{A8}$$

where γ_s is the surface energy. Typical values range between 20 MPa for $0.1 \mu\text{m}$ voids and 2 GPa for 1 nm voids. To achieve the required misfit stress, a void volume fraction $f \approx 10^{-3}$ would be needed on the as-deposited grain boundaries.

A4. Grain boundary stress

Finally, it is noted that there is a stress associated with the grain boundaries. This stress is given by

$$\sigma^R \approx \gamma_b/d. \tag{A9}$$

It is typically 1 GPa for 1 nm size grain, but only 1 MPa for $1 \mu\text{m}$ grains.